SAND2014-18219

SANDIA REPORT

####
Unlimited Release
Printed 09/2014

Multi-depth Measurement of Fast Neutrons

J. Brennan, B. Cabrera-Palmer, M. Gerling, P. Marleau, C. Roecker, M. Sweany

Prepared by
Sandia National Laboratories
Albuquerque, New Mexico 87185 and Livermore, California 94550

Sandia National Laboratories is a multi-program laboratory managed and operated by Sandia Corporation,
a wholly owned subsidiary of Lockheed Martin Corporation, for the U.S. Department of Energy's
National Nuclear Security Administration under contract DE-AC04-94AL85000.

Issued by Sandia National Laboratories, operated for the United States Department of Energy by Sandia Corporation.

Available to DOE and DOE contractors from
U.S. Department of Energy
Office of Scientific and Technical Information
P.O. Box 62
Oak Ridge, TN 37831

Telephone: (865) 576-8401
Facsimile: (865) 576-5728
E-Mail: reports@adonis.osti.gov
Online ordering: http://www.osti.gov/bridge

Available to the public from
U.S. Department of Commerce
National Technical Information Service
5285 Port Royal Rd
Springfield, VA 22161

Telephone: (800) 553-6847
Facsimile: (703) 605-6900
E-Mail: orders@ntis.fedworld.gov
Online ordering: http://www.ntis.gov/help/ordermethods.asp?loc=7-4-0#online

####
Unlimited Release
Printed 09/2014

Multi-depth Measurement of Fast Neutrons

J. Brennan, B. Cabrera-Palmer, M. Gerling, P. Marleau, C. Roecker, M. Sweany

Abstract

A spallation based multiplicity detector has been constructed and deployed to the Kimballton Underground Research Facility to measure the cosmogenic fast neutron flux anti-coincident from the initiating muon. Two of the three planned measurements have been completed (∼380 and ∼600 m.w.e) with sufficient statistics. The third measurement at level 14 (∼1450 m.w.e.) is currently being performed. Current results at ∼600 m.w.e. compare favourably to the one previous measurement at 550 m.w.e. For neutron energies between 100 and 200 MeV measurements at ∼380 m.w.e. produce fluxes between $1e^{-8}$ and $7e^{-9}$ n/cm^2/s/MeV and at ∼600 m.w.e. measurements produce fluxes between $7e^{-9}$ and $1e^{-11}$ n/cm^2/s/MeV.

Acknowledgment

This work was supported by NA-221, the office of non-proliferation R&D of the NNSA.

Contents

Appendix

List of Figures

List of Tables

Chapter 1

Introduction

The goal of the Multiplicity And Recoil Spectrometer (MARS) is to characterize the muon-induced neutron background at multiple rock overburdens. These measurements will allow the development of a depth dependent background model that will be used to determine an acceptable depth for a kilo-ton scale water Cherenkov-based nuclear reactor monitor. Of particular interest are neutrons that mimic the inverse beta decay signal resulting from antineutrino interactions in a water Cherenkov detector:

$$\overline{\nu}_e + p \rightarrow e^+ n. \tag{1.1}$$

Cosmic-ray interactions in surrounding rock and materials or in the detector itself produce showers of particles that mimic inverse beta decay: two energy deposits separated by a time characteristic of neutron capture in gadolinium-doped water. Cosmogenic fast neutrons with energies up to a few hundred MeV are concerning because they cannot be effectively vetoed and can penetrate through even the thickest detector shields, initiating secondary showers within the detector itself.

While one can deploy detectors deeper underground to reduce the rate of cosmogenic backgrounds, the cost of doing so is in many cases prohibitive, especially in the case of remote reactor monitoring in which an existing overburden may or may not exist near a particular reactor. It is therefore beneficial to determine the minimum depth at which such a detector can operate, effectively requiring the characterization of cosmic-ray induced backgrounds such as high energy neutrons.

The following sections give a description of the spallation based multiplicity detector design[1], the measurement campaign, the spectral un-folding algorithm, and a comparison of final results to other published work.

Detector and Measurement Space Design

Previously, fast neutron rate measurements have been demonstrated underground using a fast-to-slow neutron lead converter in conjunction with a neutron capture detector such as

---

[1] For more information on the detector design please see the initial design review [2].

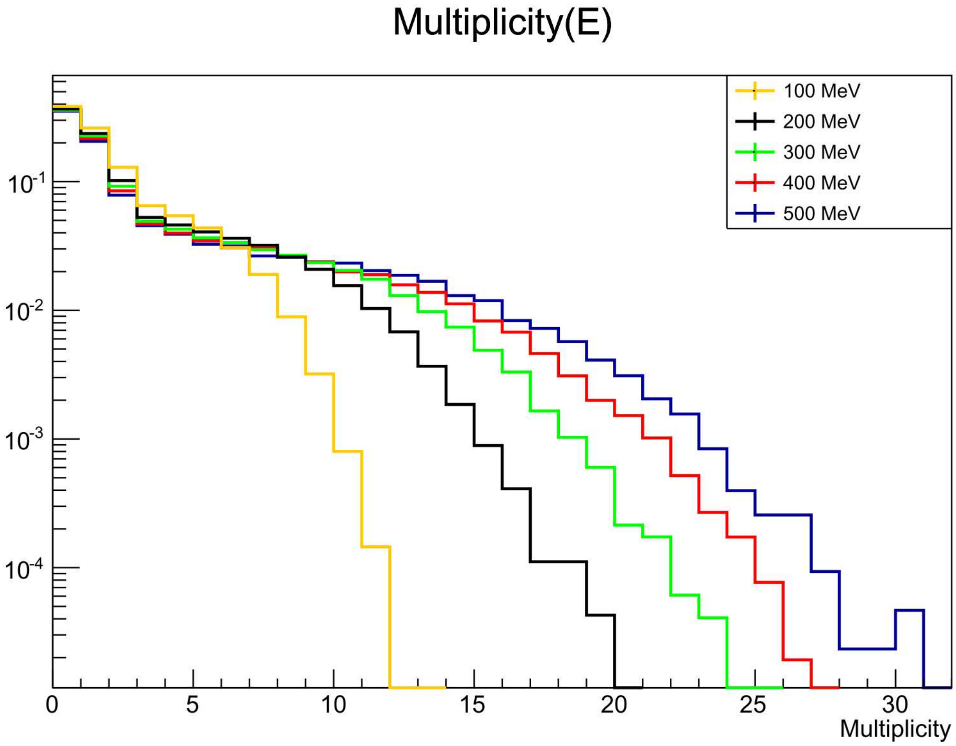

Figure 1.1: The detected multiplicity normalized to an integral of 1 for several different neutron energies. As the neutron energy increases the multiplicity increases.

a gadolinium-doped water Cerenkov detector [3, 4]. The high multiplicity showers that result from (n, kn) reactions when fast neutrons hit the lead target provides a measurement of the fast neutron rate, and allow for spectral un-folding of the neutron energy spectrum based on the shower multiplicity. This method has the advantages of low backgrounds for a sufficiently high multiplicity requirement, and is effective for neutron energies above approximately 40 MeV depending on the accidental background rates.

When a fast neutron hits a lead target, a neutron shower can develop resulting in multiple $\sim$1 MeV neutrons emerging from both the top and bottom of the target; the multiplicity of the shower is correlated with the incident neutron energy (Fig. 1.1). By using plastic scintillator sheets interleaved with gadolinium as a detection medium, these neutrons are quickly thermalized and captured. The detector response is maximized for complete shower coverage, i.e. when the lead is surrounded by active detector.

Measurement Data Space

To provide sufficient information to the spectral un-folding algorithm, multiple components of the multiplicity signal are used: the thermalization energy of all secondary neutrons entering the scintillator from the lead, the number of secondary neutron captures on Gd, and the energy of all Gd showers. Each parameter is illustrated in Fig. 1.2. In addition to the

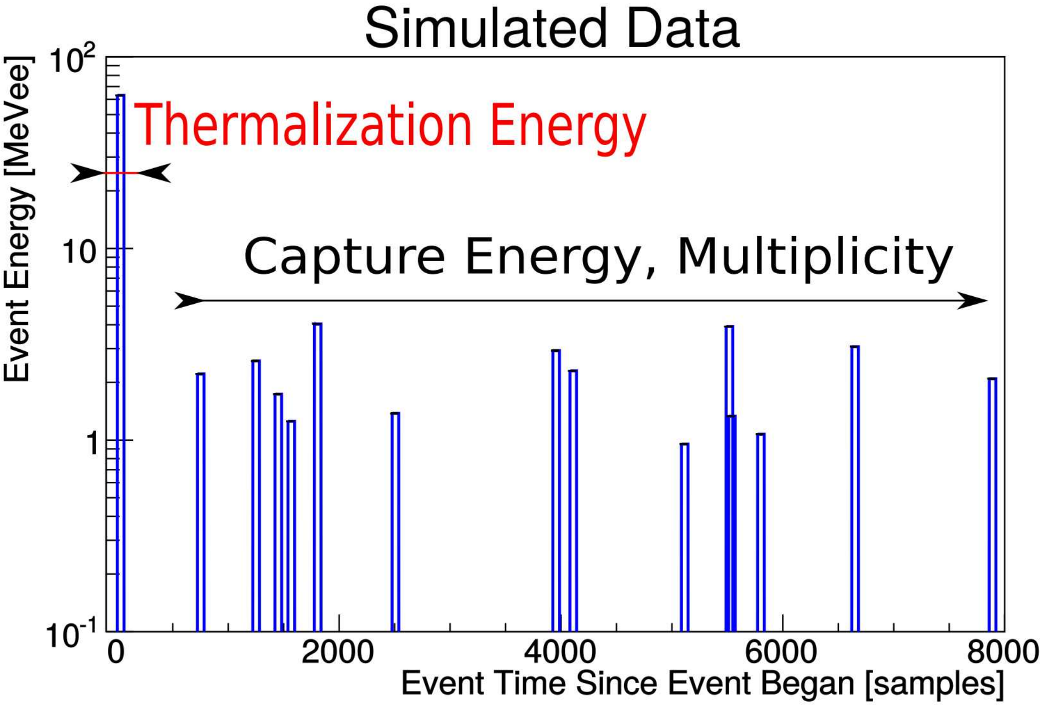

Figure 1.2: The expected structure of multiplicity events from Monte Carlo simulation. The thermalization energy is due to the secondary neutrons exiting the lead and scattering in the detector. The capture energy and multiplicity signal are due to the thermalized secondary neutrons capturing on the gadolinium. One sample is $4.1\bar{6}$ns.

incident neutron energy, these three components can be viewed as corresponding to certain event by event characteristics of the detector/neutron interaction. Because these components are correlated, the spectral unfolding becomes very complicated. The thermalization energy is recorded in one pulse, and roughly corresponds to the number of neutrons produced in the lead. The number of captures provides information on the number of neutrons in the lead as well as the detection efficiency. The capture energy provides information on the location of the incident event in the lead. The correlations between these parameters are indicated in Fig. 1.3. The capture energy rises with multiplicity. The thermalization energy is predominantly low for all multiplicities and capture energies but exhibits a high energy tail.

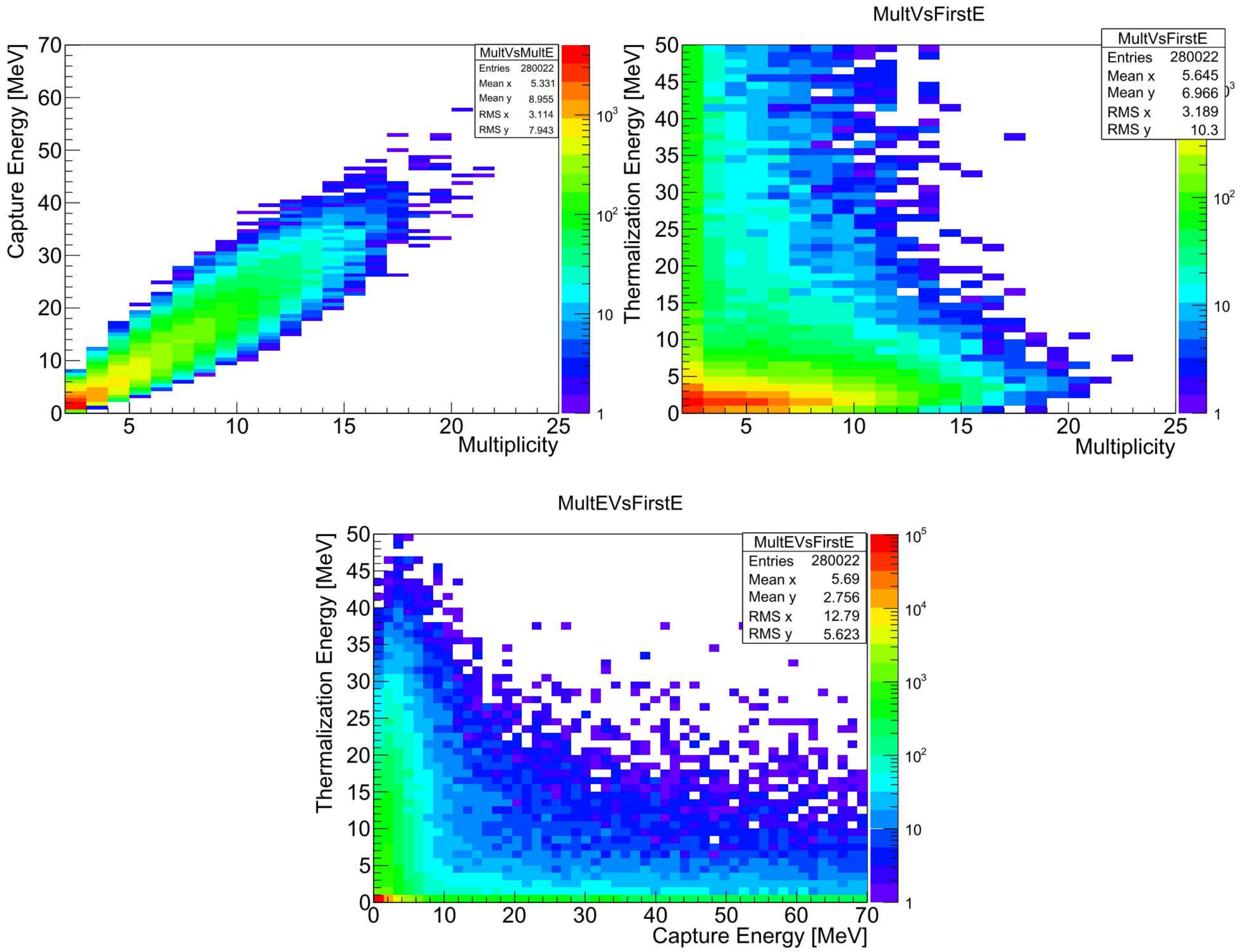

Figure 1.3: The top left is the capture energy versus the multiplicity for primary neutrons impinging upon the detector with energies between 30 and 500 MeV from Monte Carlo simulations. The top right is the thermalization energy versus the multiplicity for primary neutrons impinging upon the detector with energies between 30 and 500 MeV from Monte Carlo simulations. The bottom is the thermalization energy versus the capture energy for primary neutrons impinging upon the detector with energies between 30 and 500 MeV from Monte Carlo simulations.

In order to reject backgrounds, a minimum multiplicity requirement is enforced in addition to an energy threshold of ∼530 keV on every deposition within a multiplicity train. Additionally all depositions following the first deposition in a multiplicity train are required to have energy less than the maximum energy emitted by n-Gd captures (∼8 MeV). This requirement is intended to prevent two very high energy neutrons from interacting in the detector at the same time. Currently the un-folding is performed using a multiplicity threshold of 5, 6, and 7. The mean value and standard deviation are quoted.

In the future a separate Monte Carlo will be performed using the measured uncorrelated accidentals background rate and inter-event time in order to simulate the expected background contamination. This can be used to make a dynamic signal-to-background requirement which is dependent upon the recorded multiplicity and energy threshold, quantifying the singles contamination and recovering events which deposit small multiplicity but high energy that are indicative of incident high energy neutrons.

Physical Design

The detector is designed to optimize the collection of the aforementioned three components of the multiplicity signal. It consists of two plastic scintillator/Gd detectors with dimensions 75cm×100cm× ∼ 25cm on either side of ∼20cm of lead contained in a steel table. The plastic/Gd detectors each consist of eleven 2 cm thick BC-408 plastic scintillator sheets sandwiching layers of mylar sheets coated with a Gd loaded paint. Each end is coupled to a 4 inch acrylic light guide with eight 5 inch ADIT photo multiplier tubes (PMTs) coupled to the guides by silicon grease.

The two detectors are held together by a steel frame that is mounted to the top and bottom of a steel table that contains 75cm×100cm×20cm of lead (∼140 bricks). An exploded view of the assembly of the detectors, table, and lead are shown in Fig. 1.4, and the assembled view is shown in Fig. 1.5. The table is be bolted to the frame of the deployment platform which supports the muon veto system.

The muon veto system consists of seven 72in×24in×1in plastic scintillator paddles coupled to fishtail lightguides and PMTs on each end. These seven paddles surround the detector on the top and sides as seen in Fig. 1.6. Four more paddles with dimensions ∼ 24in× ∼ 24in×2in cover the ends of the detector. Each of these is coupled to a single PMT on the face of the paddle. All paddles include at least four inches of overlap to ensure as close to total coverage as possible. The fully assembled muon veto system is shown in Fig. 1.7.

Triggering Algorithm

To identify correlated multiplicity events in a background of uncorrelated singles events, a unique trigger was constructed. Instead of having a fixed gate length which can reduce

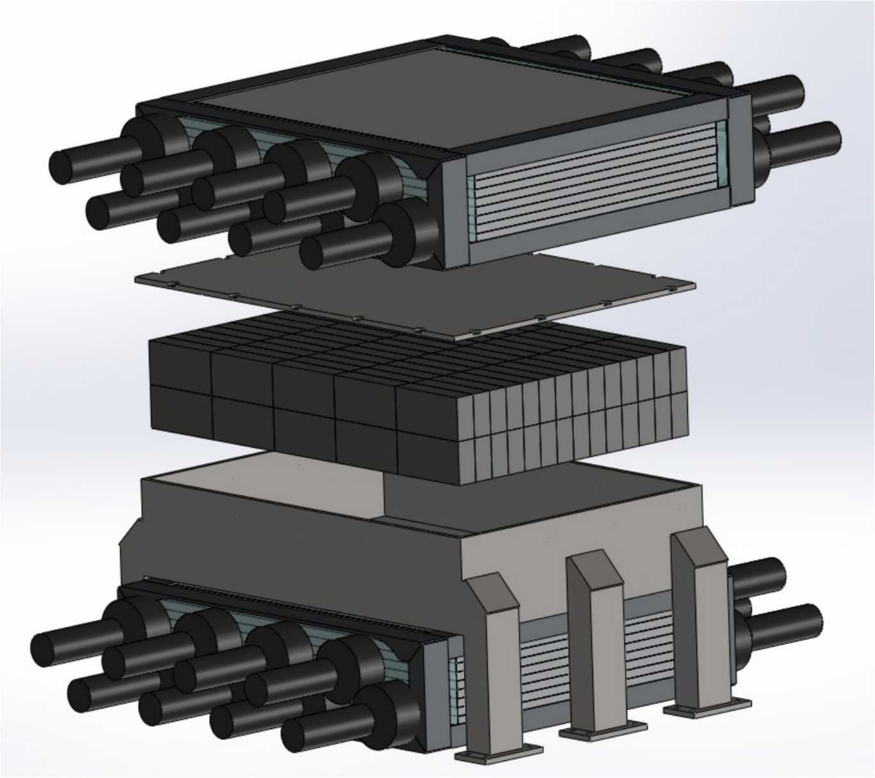

Figure 1.4: Exploded view illustration of the detectors, frame, and lead.

our detection efficiency for events with large multiplicities, an expanding gate was used. The trigger requires 3 depositions, individually above an energy threshold within 65μs. If this trigger is recorded then the gate is extended an additional 65μs from the second to last deposition in the train. The gate continues increasing until no new depositions are detected. The multiplicity train data considers the top and bottom detector to be two separate detectors and does not consider individual PMT signals. However the triggering algorithm ignores this information.

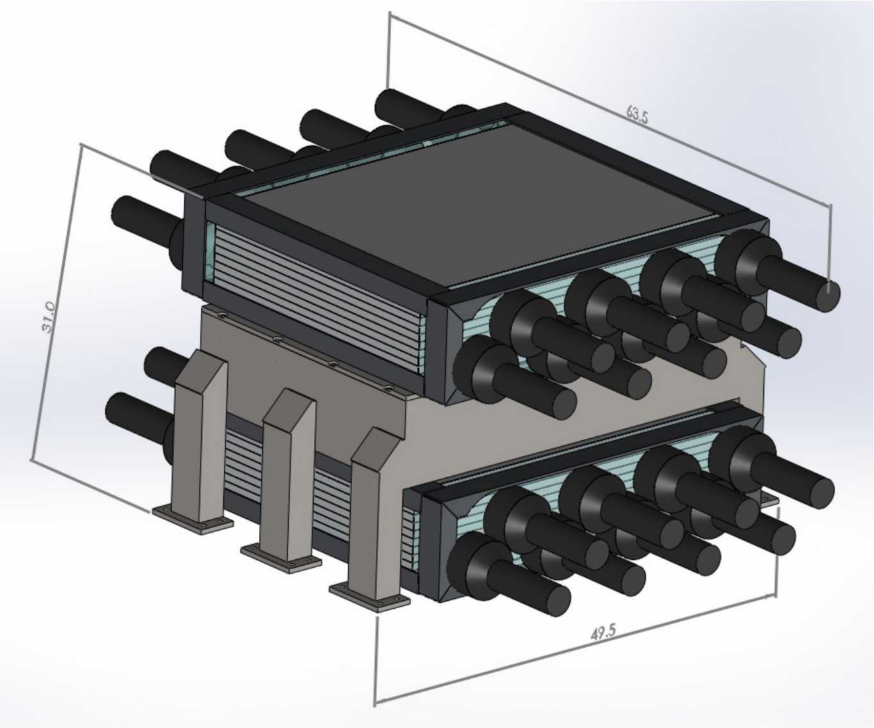

Figure 1.5: Illustration of the assembled detectors, frame, and lead including overall dimensions in units of inches.

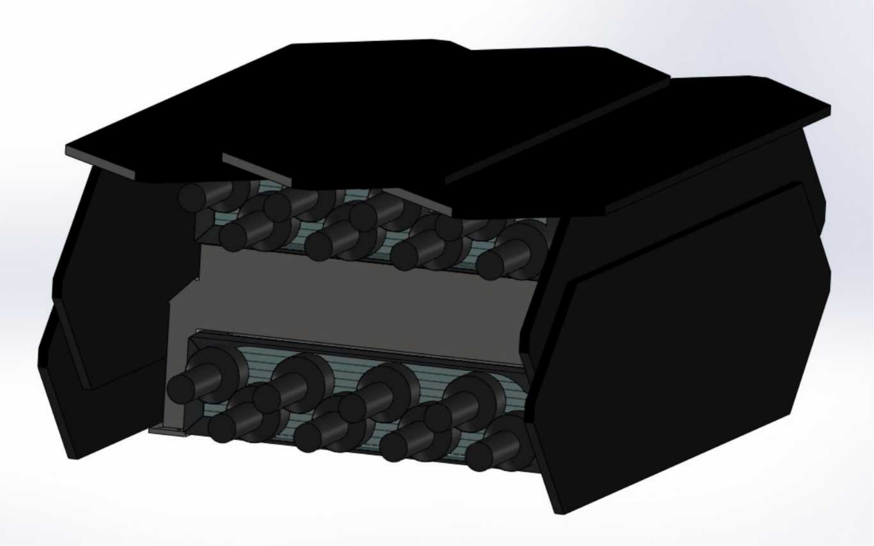

Figure 1.6: End view of assembled detector showing the six 72 in. paddles. The end paddles have been removed.

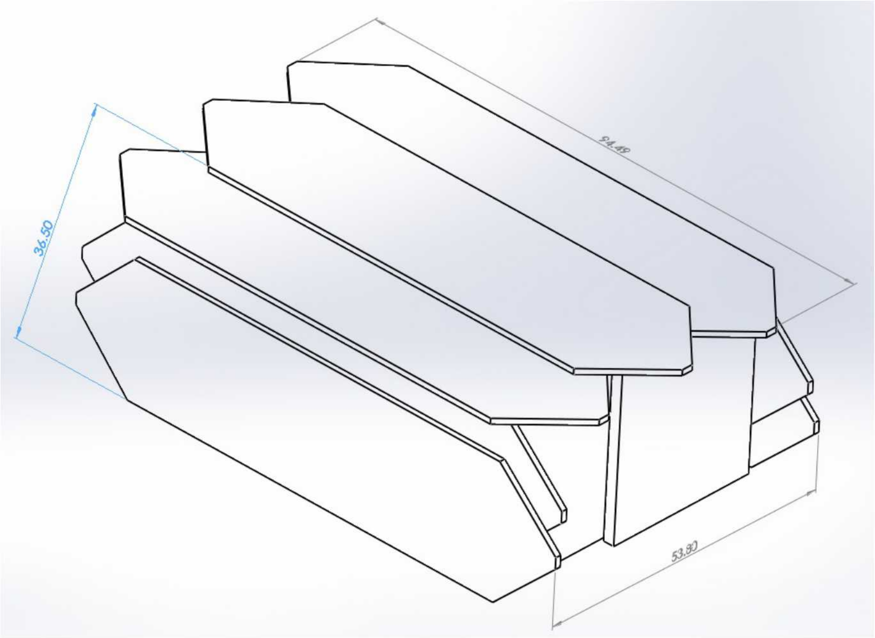

Figure 1.7: Illustration of the full muon veto system including dimensions in units of inches.

Chapter 2

Measurement Campaign

Three measurements were planned at ∼380, ∼600, and ∼1450 m.w.e. at the Kimballton Underground Research Facility (KURF) near Giles, Virginia. The two shallow measurements have been completed and the deepest measurement is ongoing. The detector has been operating since late May 2013. It first operated for a week above ground. However the muon veto energy thresholds that were used were relatively high so this data is likely muon contaminated to some degree. Once the detector was deployed underground, the thresholds were lowered to improve the veto efficiency. Data will be taken on the surface upon completion of all subterranean measurements allowing for a cross check to the abundant surface neutron spectra measurements. From June to December 2013 the detector operated at level 6 of KURF (∼600 m.w.e.) with a slow but steady decrease in individual PMT gain (Appendix A). High voltage problems were persistent. Stable operation was achieved upon replacement of the high voltage system in late June 2013. Gamma and neutron calibrations were performed before and after a move in December 2013 to level 2 of KURF (∼380 m.w.e.). High voltage problems again contributed to down time until January 2014. From January until May 2014 the detector operated in a relatively stable configuration with another slight decrease in PMT gain. Gamma and neutron calibrations were again performed before and after a move in May 2014 to the level 14 of KURF (∼1450 m.w.e.). The detector has been operating since May 2014 at level 14 of KURF and will continue to operate there until funding runs out.

Energy Calibration

To create a conversion from measured detector units to energy, calibrations were performed regularly with a Cf-252 and Th-232 source. The calibration setup adjusted one side of the side veto panels to allow the sources near both detectors. The Cf-252 calibration used a small and fast plastic scintillator to tag the fission gammas coming from the source. To record a signal the multiplicity trigger must be initiated requiring greater than 2 depositions in 65 μs coincident with the tag detector. Any deposition's energy after the second deposition was recorded. The Th-232 calibration used the total energy spectra without the multiplicity trigger. Both spectra were background subtracted using their respective triggering algorithm without a source present. The calibration configuration was simulated with a Monte Carlo simulation. A χ^2 minimization is performed using a Gaussian smear of the simulated data and a polynomial function to create a conversion from digitized PMT pulses to energy (Fig.

2.1).

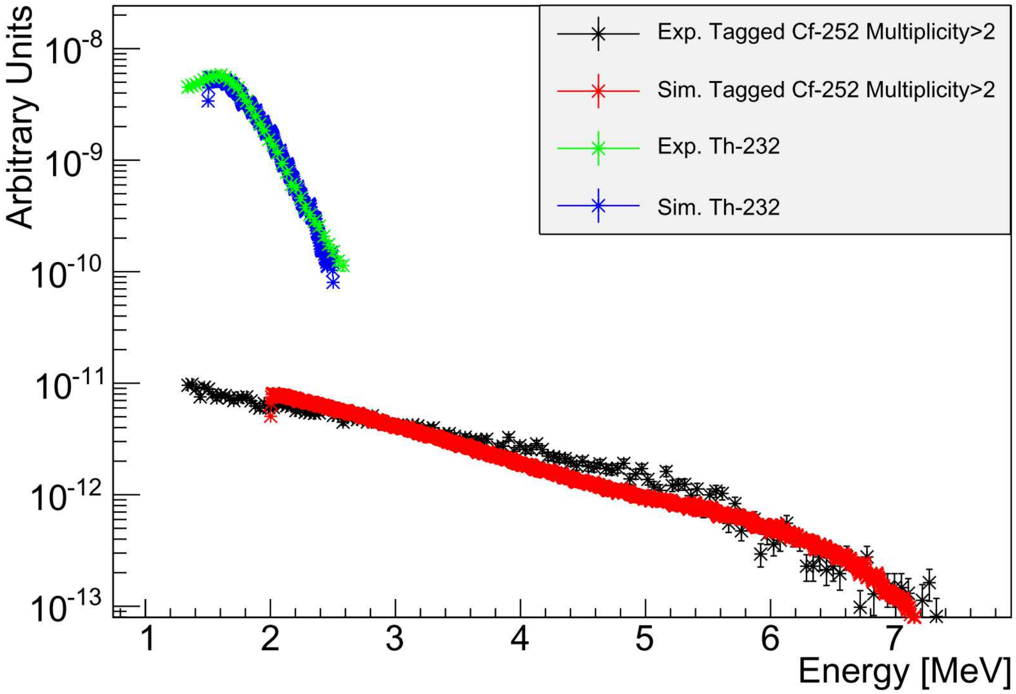

Figure 2.1: The energy calibration from late April 2014 at level 2. A Cf-252 and Th-232 source were used by opening one of the veto panels and placing the source as close as possible to the top detector. The Cf-252 measurement has a small plastic scintillator to act as a tag and requires a tag and a multiplicity greater than 2 to be recorded. The Th-232 calibration is the background subtracted energy spectrum.

Removing Muon Correlated Events

To remove muon correlated showers from the multiplicity data the time since veto trigger was investigated in the first several months at level 6 (Fig. 2.2). It can be seen in Fig. 2.2 that a time since last muon window of 200μs should reduce reject muon correlated events to less than one per 4 months of dwell time. To test the validity of this veto length the window was varied to longer values and the multiplicity event rate was found to be stable. This same test was performed on level 2 with similar results.

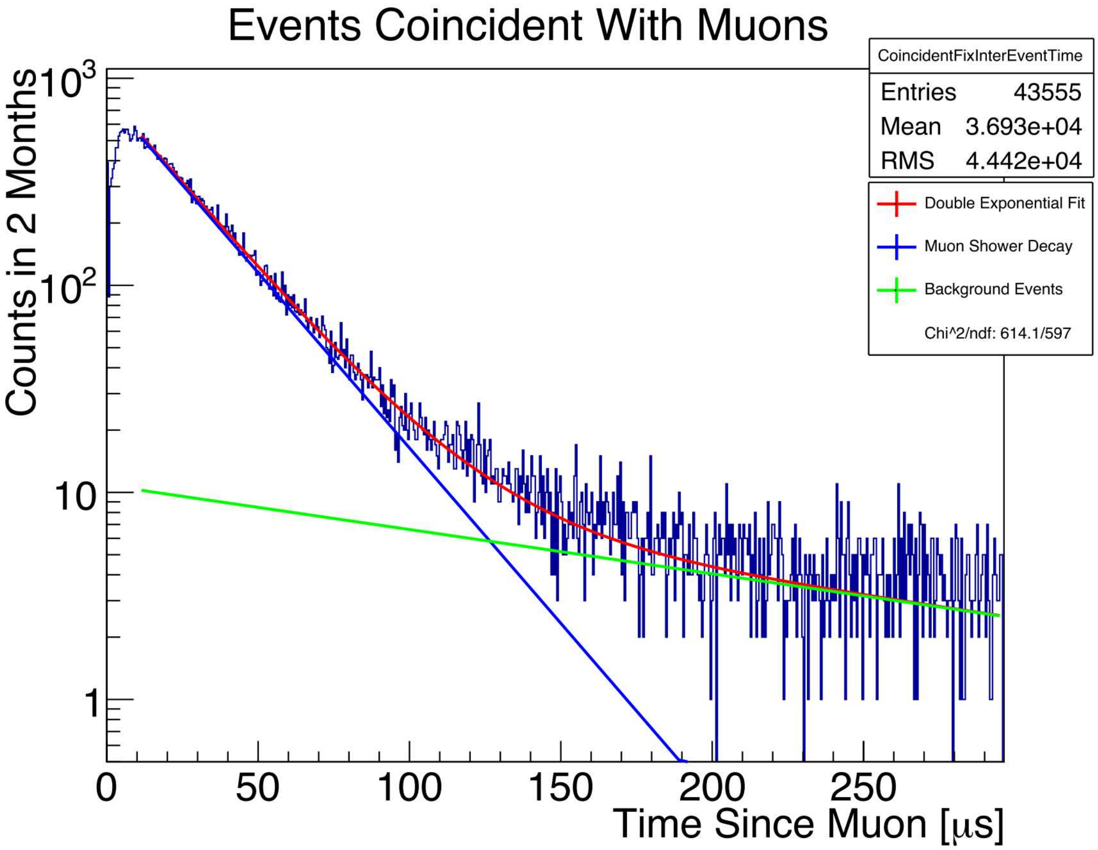

Figure 2.2: The time since muon of events which initiate the multiplicity trigger in the first several months at level 6. This plot is designed to test the die-out time of a muon shower in the detector. The blue histogram is the data, the blue line is the fit to the muon correlated data, the green line is the fit to the background data, and the red line is the sum of both fits.

Chapter 3

Spectral Un-Folding

The neutron spectrum is un-folded using Maximum-Likelihood Expectation-Maximization (MLEM)[5]. MLEM is part of a subset of very similar algorithms that are designed to solve inverse (non-direct) problems. These algorithms are designed to solve problems in which the desired variable cannot be directly measured, but instead a correlated variable is measured and the most probable distribution of the desired variable is inferred. In MARS the neutron energy is not directly measured, but rather a set of parameters correlated to the neutron energy are measured. This algorithm finds the most likely distribution of neutron energies that could have produced the measured parameters given a detector response matrix that is estimated using a Monte Carlo model of the detector.

Un-Folding Algorithm

To solve for the incident neutron spectrum, the inverse problem must solve the Fredholm first-kind integral equation

$$g(\vec{y}) = \int A(E,\vec{y})f(E)dx + b(\vec{y}), \tag{3.1}$$

where $g(\vec{y})$ is the measured output, $A(E,\vec{y})$ is the kernel from simulation[1], $f(E)$ is the desired output, $b(\vec{y})$ is the background, $\vec{y}$ is the vector of measured parameters, and E is the energy. Because the continuous form of $g(\vec{y})$ and $A(E,\vec{y})$ is not known, Eq. 3.1 must be discretized

$$\vec{g}_{meas} = \mathbf{A}\vec{f} + \vec{b}. \tag{3.2}$$

The problem is that **A** is most likely singular (ill-conditioned), removing the possibility of direct inversion. To solve for $f(E)$ an iterative approach is used, where k is the iteration number:

Iterative Inverse Algorithm

1. Guess $\vec{f}^k$

---

[1] Alternatively called the response/system matrix

2. Calculate $\vec{g}^{k}_{pred} = \mathbf{A}\vec{f}^{k}$

3. Compare $\vec{g}^{k}_{pred}$ to $\vec{g}_{meas}$

4. Update to $\vec{f}^{k+1}$

5. Go to Step 2, where k=k+1

Un-Regularized MLEM

MLEM is a well developed approach to proceed through the previously described iterative algorithm. It includes a noise model called a likelihood function to create the update step

$$L(E, \vec{y}) = \prod_{i=0}^{i<n} P\Big(g_{meas,i} \mid g_{pred,i}\Big), \tag{3.3}$$

where P is the probability dictated by the statistics of each predicted bin, given the measured bin, of the one dimensional column vector $\vec{g}$. This is a counting experiment observing Poisson statistics:

$$P\Big(g_{meas,i} \mid g_{pred,i}\Big) = \Big(e^{-(g_{pred,i})}\Big)\frac{\Big(g_{pred,i}\Big)^{g_{meas,i}}}{(g_{meas,i})\,!}, \tag{3.4}$$

which produces a likelihood that can be converted to a summation by using the negative logarithm of Eq. 3.3

$$\Psi(E, \vec{y}) = -ln\Big(L(E, \vec{y})\Big) = \sum_{i=0}^{i<n} g_{pred,i} - g_{meas,i} * ln(g_{pred,i}), \tag{3.5}$$

where the background term $\vec{b}$ and another constant term have been dropped. The background is assumed to be small or must be subtracted from the measured data. The constant term is dropped because the algorithm is looking for a peak in likelihood space and adding a constant to the whole space does not control the position of the peak. To derive the update equation from Eq. 3.5 there are two approaches: a statistical argument [5] or a mathematical surrogate function which bounds the likelihood function [6]. The agreed upon answer however is

$$f_j^{k+1} = \frac{f_j^k}{\sum_{i=1}^{n} \mathbf{A}_{ij}} \sum_{i=1}^{n} \mathbf{A}_{ij} \frac{g_{meas,i}}{g_{pred,i}}. \tag{3.6}$$

The advantage to the above algorithm over other update algorithms[2] is that it ensures montonicity and non-negativity of f. Montonicity ensures that the likelihood is increasing in each iteration. Non-negativity of f enforces a positive (physical) flux at every energy.

While Eq. 3.6 provides a starting place for solving Eq. 3.2 there exist problems with the solution. Over-convergence is the most serious problem, which results in an oscillatory

---

[2] For example the Newton-Rapheson.

solution. To alleviate the problem, a regularization can be applied to avoid the non-physical oscillations in the reconstructed spectrum f. The regularization applied to the MARS un-folding is described in Appendix C. Additional information is presented about filling the kernel ($\mathbf{A}$) and including the intrinsic efficiency into the MLEM in Appendix B.

Simulated Spectra Un-Folding

Four energy distributions were simulated to test the ability of the measured data space and Eq. C.5 to reconstruct a simulated energy spectrum. The first distribution was predicted by Wang[7], and later by Mei and Hime, [8]. This distribution is intended to be valid for depths greater than 1500 m.w.e. with no indication that the results can be extrapolated to the depths meaured by MARS. The final three spectra (Perkins, Hayakawa, and Katrin) are parameterizations described in the Palo Verde Reactor Monitoring experiment progress review [9] and are the experimental results of other very shallow depth rare event searches. These distributions are intended to be valid for shallower depths than measured by MARS. with no indication that the results can be extrapolated to the depths meaured by MARS. All spectra were simulated in Geant4.9.6.p02 using the MENATE_R data for high energy neutron-carbon interactions. For each simulation the optimal regularization parameter was determined using the L-Curve method (Appendix D.0.5). After determining the optimal regularization parameter the simulated data space ($\vec{g}$) was Poisson sampled and the algorithm was run 200 times to generate error bars.

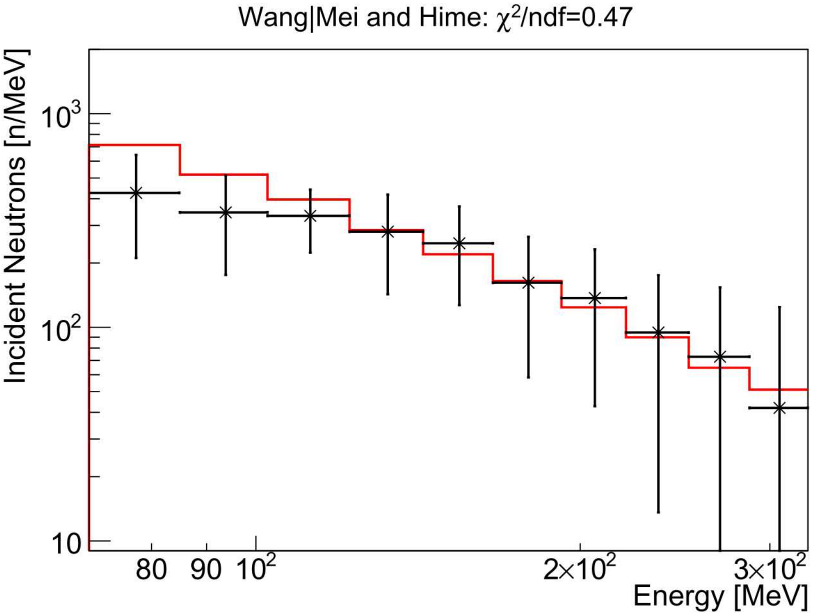

Figure 3.1: The incident spectra thrown from the walls normalized for the energy bin width versus the energy for the Wang or Mei and Hime distribution. The red histogram is the simulated spectra and the black points are the un-folded distribution. Error bars on the points are due to Poisson sampling the simulated measured data space.

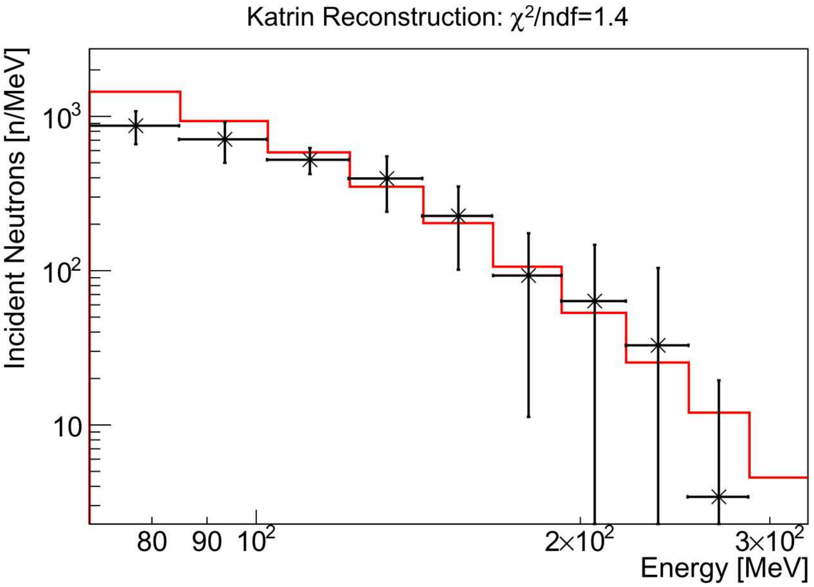

Figure 3.2: The incident spectra thrown from the walls normalized for the energy bin width versus the energy for the Katrin prediction. The red histogram is the simulated spectra and the black points are the un-folded distribution. Error bars on the points are due to Poisson sampling the simulated measured data space.

Across all simulated spectral shapes, a systematic under prediction exists below 100 MeV. This can most likely be attributed to poor statistics in the kernel matrix **A** at low energies due to the multiplicity 6 requirement. If low statistics is the problem it can be alleviated by generating more events for the kernel, or changing the energy binning, lowering the multiplicity requirement, or quoting the systematic error. However the algorithm does an acceptable job at reconstructing incident neutron energies between 100 and 300 MeV, which is the primary concern of this analysis for large water-Cherenkov detectors.

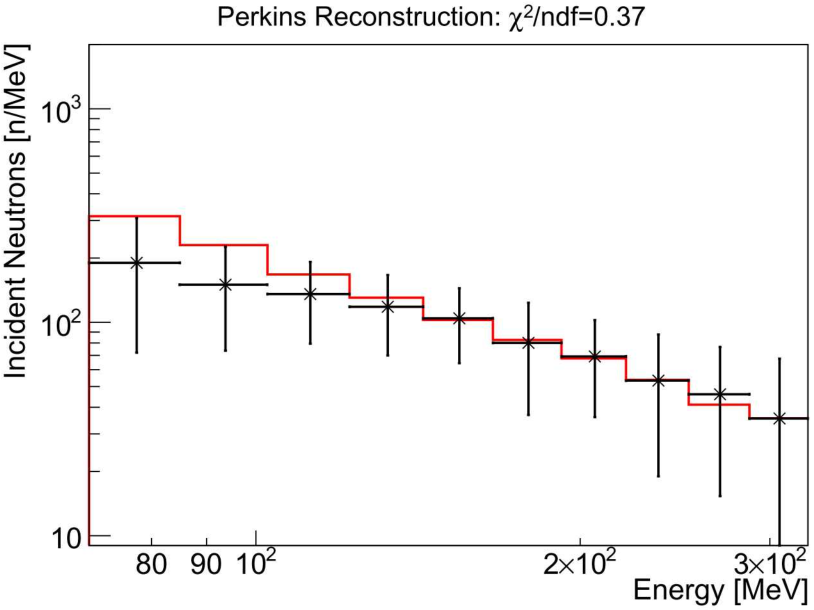

Figure 3.3: The incident spectra thrown from the walls normalized for the energy bin width versus the energy for the Perkins prediction. The red histogram is the simulated spectra and the black points are the un-folded distribution. Error bars on the points are due to Poisson sampling the simulated measured data space.

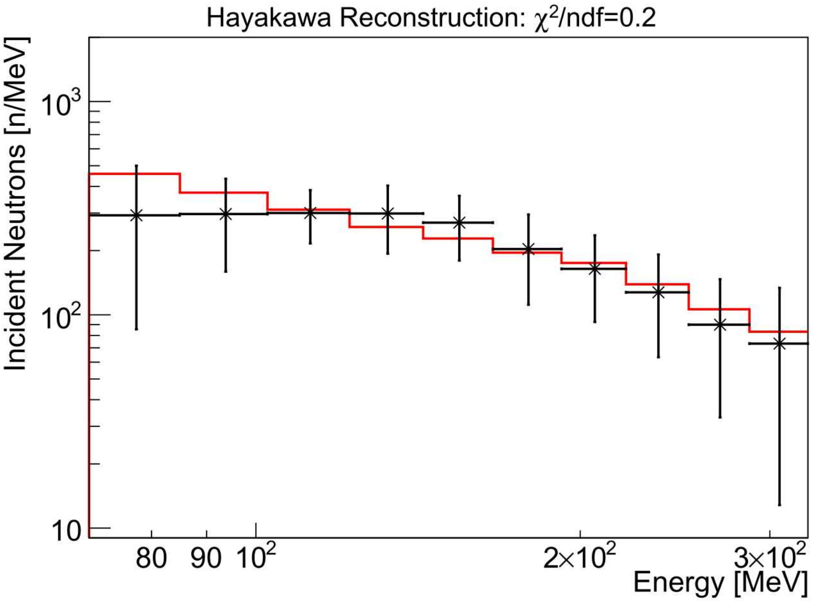

Figure 3.4: The incident spectra thrown from the walls normalized for the energy bin width versus the energy for the Hayakawa prediction. The red histogram is the simulated spectra and the black points are the un-folded distribution. Error bars on the points are due to Poisson sampling the simulated measured data space.

Chapter 4

Results

Presented here are the results from level 2 and 6 of KURF. Sufficient statistics have not yet been achieved at level 14. All results have error bars which are only a function of Poisson sampling the measured data space. This does not include other sources of error: energy calibration, background contamination above multiplicity 5, position dependent light response in the detector, etc. We anticipate that these results will be close to the final answer, but our understanding of the systematic uncertainties will improve with further study. To this end, different multiplicity requirements are are used to estimate the reconstruction uncertainty. Multiplicity requirements of 5, 6, 7, and 8 (if statistics permit) are used to represent the highest, most probable, and lowest expectation from the data. If all systematic effects were completely accounted for, each multiplicity requirement should reconstruct the same spectrum. Deviations are an indication of systematic uncertainty in the detector response. An energy requirement of 530 keV is used for each deposition in a multiplicity train.

Data and Spectral Un-Folding

Using the same unfolding algorithm as the simulated cases the experimental data is converted into units of flux (n/cm^2/s/MeV, Appendix E). Ideally the analysis would use angular flux or intensity to quote the final results. However in an effort to compare to other works the results here will be in flux. Level 2 results are shown in Fig. 4.1. Regardless of the multiplicity requirement the un-folding algorithm predicts a flux varying between 3e^{-8} to 9e^{-9} n/cm^2/s/MeV at 100 MeV and between 1e^{-8} to 1e^{-9} n/cm^2/s/MeV at 200 MeV. Level 6 results are shown in Fig. 4.2 and exhibit more sensitivity to the multiplicity requirement than the level 2 results. While varying the multiplicity requirement from 5 to 7 the unfolding algorithm predicts a flux varying between 2e^{-8} to 1e^{-10} n/cm^2/s/MeV at 100 MeV and between 1e^{-10} to 1e^{-11} n/cm^2/s/MeV at 200 MeV.

The lack of sensitivity at level 2 to the multiplicity requirement is probably due to much greater statistics than level 6 (on the order of a magnitude more) with a very similar gamma contamination. This is primarily due to the neutron flux being much higher while the muon veto time per muon stays the same and the gamma background stays the same resulting in a higher signal to noise. This means that the un-folding on level 6, particularly for multiplicity 5 is most likely too high. The sensitivity to multiplicity requirement requires further study as previously mentioned in section 1.

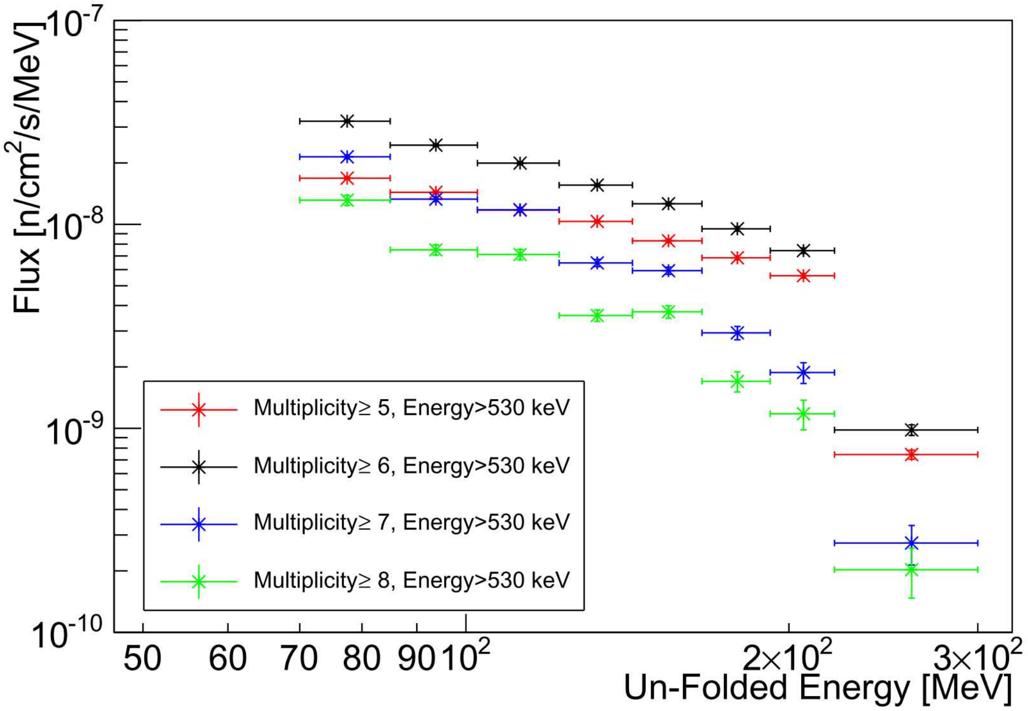

Figure 4.1: Level 2 un-folding results for multiplicity cuts of 5, 6, 7, and 8 in red, black, blue, and green respectively. The error bars are generated by Poisson sampling the measured data space and running the reconstruction 200 times.

Comparison to Other Works

Only a few other experiments have measured a neutron spectrum or integral rate at depths >100 m.w.e. anti-coincident from the initiating muon [1, 3, 4]. Of these experiments only one is inside of the overburden range being measured here and the original work is in Russian. Using a translation of the original paper an integral flux rate between 20 and 80 MeV is given for a depth of 550 m.w.e. as 2.3e^{-4} n/m^2/s [1]. Two of the same authors more recently published a paper citing that work and including the measured flux shape in arbitrary units from the original work [10](Fig. 4.3). Here we compare the mean un-folding of multiplicity 5, 6, and 7 presented in previous section to the Russian data. The data from this experiment which is at ∼600 m.w.e. is very close to the data previous measurement from Malgin et. al.

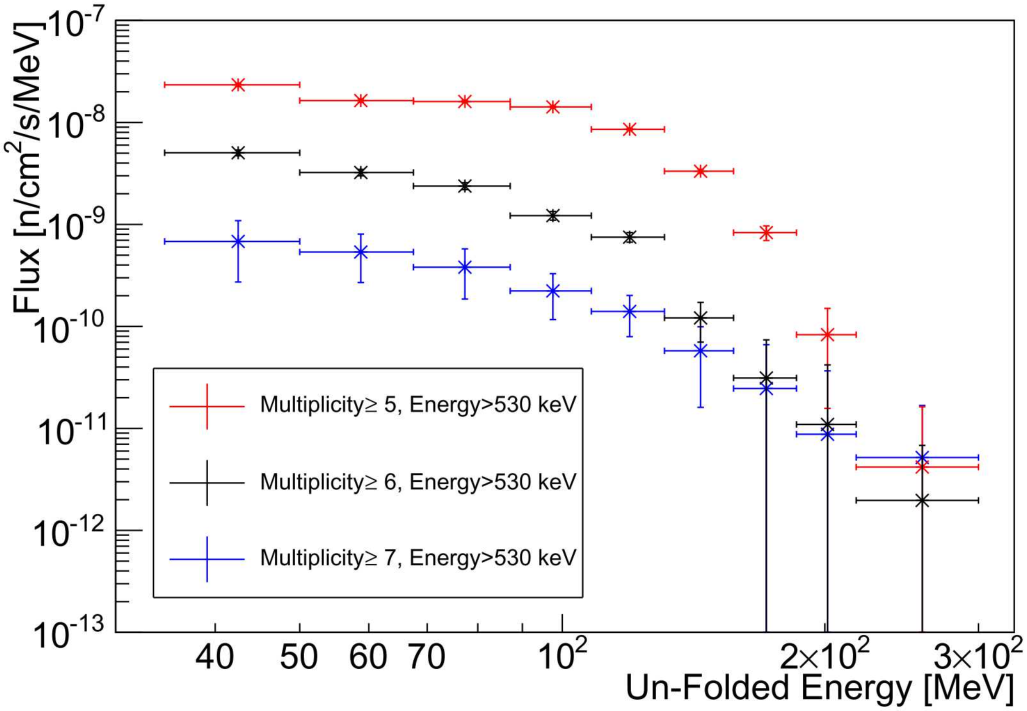

Figure 4.2: Level 6 un-folding results for multiplicity cuts of 5,6, and 7 in red, black,and blue respectively. The error bars are generated by Poisson sampling the measured data space and running the reconstruction 200 times.

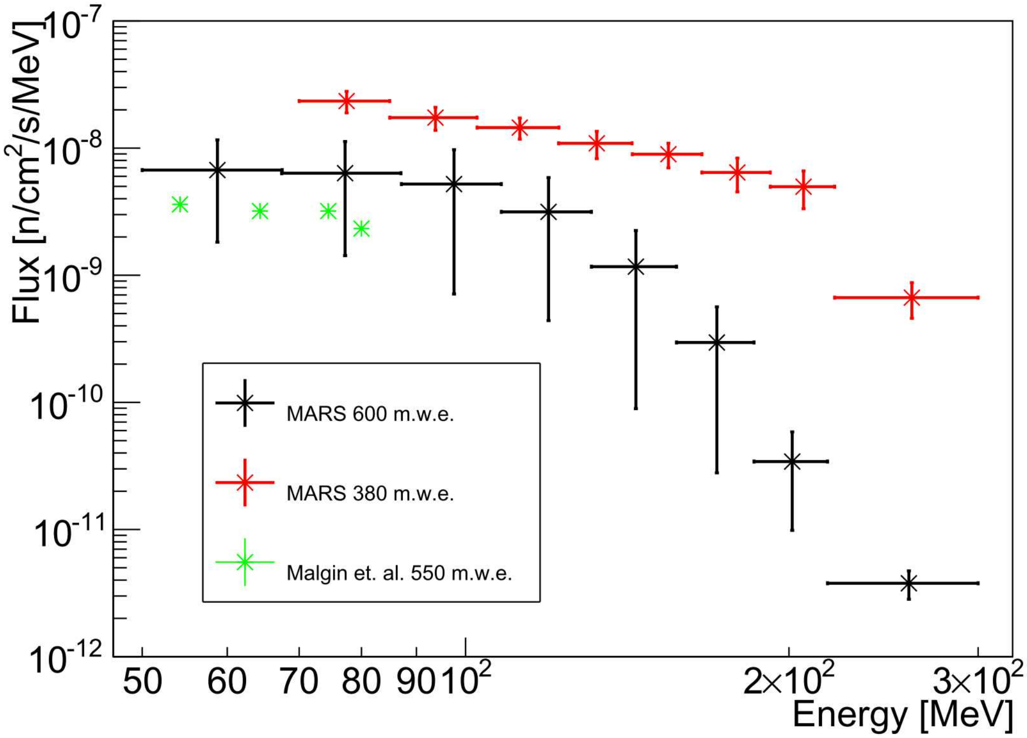

Figure 4.3: The current best measurements from this work for level 2 and 6 (∼380 and /*sim*600 m.w.e.) are compared to the data from Malgin et. al. at 550 m.w.e. Initial agreement at level 6 is encouraging. Malgin et. al. did not include error bars.

Chapter 5

Conclusion and Future Work

A spallation based multiplicity detector has been constructed and deployed to the Kimballton Underground Research Facility. Two of the three planned measurements have been completed ($\sim$380 and $\sim$600 m.w.e) with sufficient statistics. The third measurement at level 14 ($\sim$1450 m.w.e.) is currently underway. Gain drift and energy calibrations have been periodically performed. An un-folding algorithm has been created to transform the measured multiplicity data into a reconstructed energy spectrum. Current results at level 6 ($\sim$600 m.w.e.) compare favourably to the one previous measurement at 550 m.w.e. For the neutron energies relevant for water Cherenkov-based antineutrino detectors the measurements at $\sim$380 m.w.e. produce fluxes between $1e^{-8}$ and $7e^{-9}$ n/cm^2/s/MeV and at $\sim$600 m.w.e. measurements produce fluxes between $7e^{-9}$ and $\sim 1e^{-11}$ n/cm^2/s/MeV.

Significant work remains to reduce systematic uncertainties, however preliminary data analysis and un-folding are promising. A dynamic multiplicity and energy threshold with a constant signal to background value must be produced. This should have the effect of increasing the statistics and improving all measurements. With increased statistics reconstructions may extend to even higher energies than what has been presented here. Further work will include studies to better understand sources of systematic uncertainties.

References

[1] A.s. Malgin, O.g. Ryazhskaya, V.g. Ryasnyi, and F.f. Khalchukov. HIGH-ENERGY HADRONS PRODUCED BY COSMIC RAY MUONS IN THE EARTH AS A SOURCE OF BACKGROUND IN PROTON DECAY EXPERIMENTS. *JETP Lett.*, 36:376–379, 1982.

[2] N.S. Bowden, J. Brennan, D. Dobie, P. Marleau, C. Roecker, M. Sweany, and K. Weinfurther. Multi-depth measurement of fast neutrons. Internal Design Review.

[3] M. Sweany. *Characterization of Neutron Backgrounds for Direct Dark Matter Searches.* PhD thesis, University of California at Davis, 2011.

[4] Raul Hennings-Yeomans and D.S. Akerib. A Neutron Multiplicity Meter for Deep Underground Muon-Induced High Energy Neutron Measurements. *Nucl.Instrum.Meth.*, A574:89–97, 2007.

[5] L.A Shepp and Y. Vardi. Maximum likelihood reconstruction for emission tomography. *Medical Imaging, IEEE Transactions on*, 1(2):113–122, Oct 1982.

[6] AR. De Pierro. On the relation between the isra and the em algorithm for positron emission tomography. *Medical Imaging, IEEE Transactions on*, 12(2):328–333, Jun 1993.

[7] Y.F. Wang, V. Balic, G. Gratta, A. Fasso, S. Roesler, et al. Predicting neutron production from cosmic ray muons. *Phys.Rev.*, D64:013012, 2001.

[8] Dongming Mei and A. Hime. Muon-induced background study for underground laboratories. *Phys.Rev.*, D73:053004, 2006.

[9] F. Boehm. The palo verde experiment: Review of progress.

[10] A.S. Malgin and O.G. Ryazhskaya. Neutrons from muons underground. *Physics of Atomic Nuclei*, 71(10):1769–1781, 2008.

[11] A.N. Tikhonov and V.Y. Arsenin. *Solutions of Ill-Posed Problems.* Winston, Washington, DC, 1977.

[12] AR. De Pierro. A modified expectation maximization algorithm for penalized likelihood estimation in emission tomography. *Medical Imaging, IEEE Transactions on*, 14(1):132–137, Mar 1995.

[13] J. A. Fessler. Iterative methods for image reconstruction. isbi tutorial. `http://web.eecs.umich.edu/~fessler/papers/files/talk/08/isbi-notes.pdf`, 2008.

[14] Per Christian Hansen. Analysis of discrete ill-posed problems by means of the l-curve. *SIAM Rev.*, 34(4):561–580, December 1992.

[15] J.D. Sullivan. Geometric factor and directional response of single and multi-element particle telescopes. *Nuclear Instruments and Methods*, 95(1):5 – 11, 1971.

Appendix A

Gain Correction

A.0.1 Motivation

Before starting data acquisition at level 6 in June 2013, all 16 PMT channels of each of the 2 plastic scintillators were gain matched and set to cover an energy range to about 20MeV. Due to the environmental conditions in the mine, a combination of performance degradation of the High Voltage (HV) modules and optical decoupling of the PMTs and/or lightguides from the detector caused the PMT gains to decrease over time. To illustrate the gain shifts of several PMT channels, energy histograms of detector events in coincidence with muon veto events are shown in Figs. A.1 and A.2. As can be observed in Figs. A.1 and A.2, the muon bump recedes to lower values of energy as time progresses.

The gains shifts are different for each PMT channel. Since the detector energy is computed as the sum of the PMT energies, correcting each individual PMT gain to restore gain matching among all channels is necessary. Moreover, shifts in gain affect the values of energy thresholds, which cause changes in the neutron capture efficiency. This impacts the multiplicity spectrum since the probability of seeing a multiplicity M event is given by

$$P_M = \epsilon^M \left(1 - \epsilon^{(N-M)}\right), \tag{A.1}$$

where ϵ is the detection efficiency and N is the total number of neutrons produced.

A.0.2 Method and Analysis

To quantify the gain shifts, we take advantage of the muon bump of the muon-tagged event histograms shown above, as that represents a spectral feature that is present in each separate PMT channel. The time scale of the gain drifts is slow enough over several days, and thus, histograms of weekly data with the needed statistics can be used for the gain drift characterization.

We then added the first week of stable data at level 6, starting on June 27, 2013, to create template graphs for each PMT channel. These 32 templates, parametrized by an x-axis and a y-axis scale factors, are fitted to the remaining of the data grouped in week intervals. The resulting fit values the for x-axis scale factor represent a gain correction $\mathrm{g}_C^i(\mathrm{t})$ of data at time

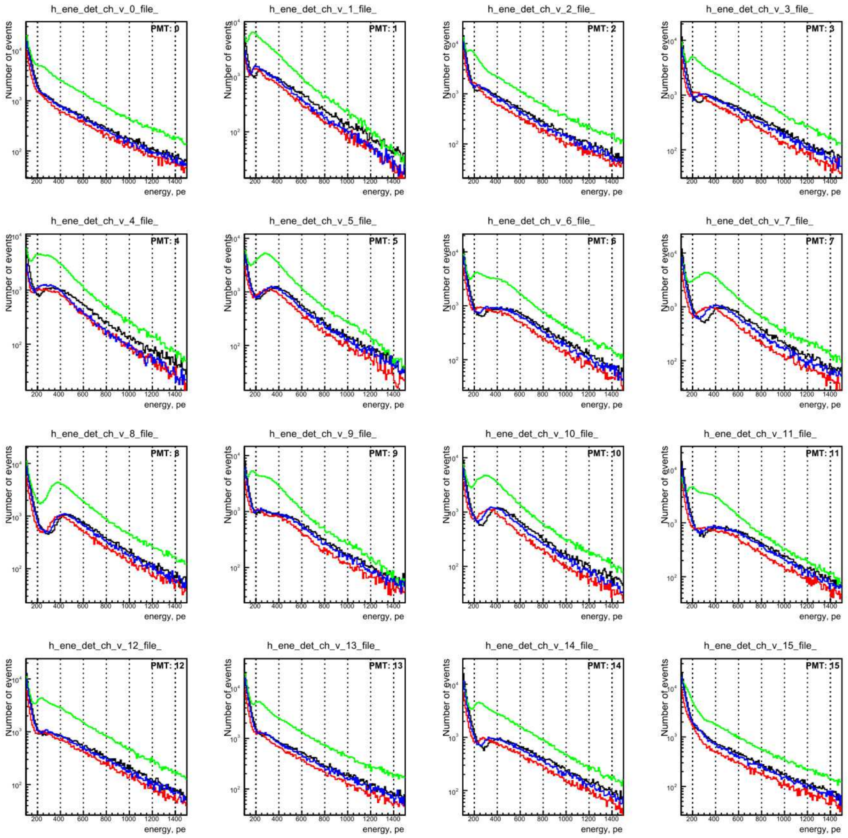

Figure A.1: Energy histograms of muon-tagged events recorded by individual PMT channels for 3 separate weeks: from June 27 to July 3, 2013 on level 6, in black; from September 25 to October 1, 2013 on level 6, in red; from January 24 to January 30, 2014 on level 2, in green. Each of those week data corresponds to what later will be identified in the text as templates T1, T2, and T3 respectively.

t with respect to the start value of the gain in week one $\mathrm{G}^i(t_0)$, so that we get the corrected i-th PMT energy as:

$$E_i^{corrected}(t) = g_C^i(t)E_i(t) = g_C^i(t)G_i(t)S_i(t_0) = G_i(t_0)S_i(t_0) \tag{A.2}$$

where $\mathrm{E}_i(\mathrm{t})$ is the measured channel energy and $\mathrm{S}_i(\mathrm{t}_0)$ is the what would be the PMT energy signal with hypothetical unit gain. Since the gains Gi(t) are generally drifting to smaller values with respect to their initial values, the gain corrections giC(t) should be larger than one.

The shape of the muon bump in the spectra differs among PMT channels. Typically, PMT channels closer to the center of the detector have well defined and prominent muon bumps, while the channels near the edges would have smaller or flatter muon bumps. Also, four PMT channels show a double-hump around the muon energies, indicating problems with light collection. Despite this variability from channel to channel, the individual shapes of the spectra for each PMT are in general maintained even while the gains are drifting, which

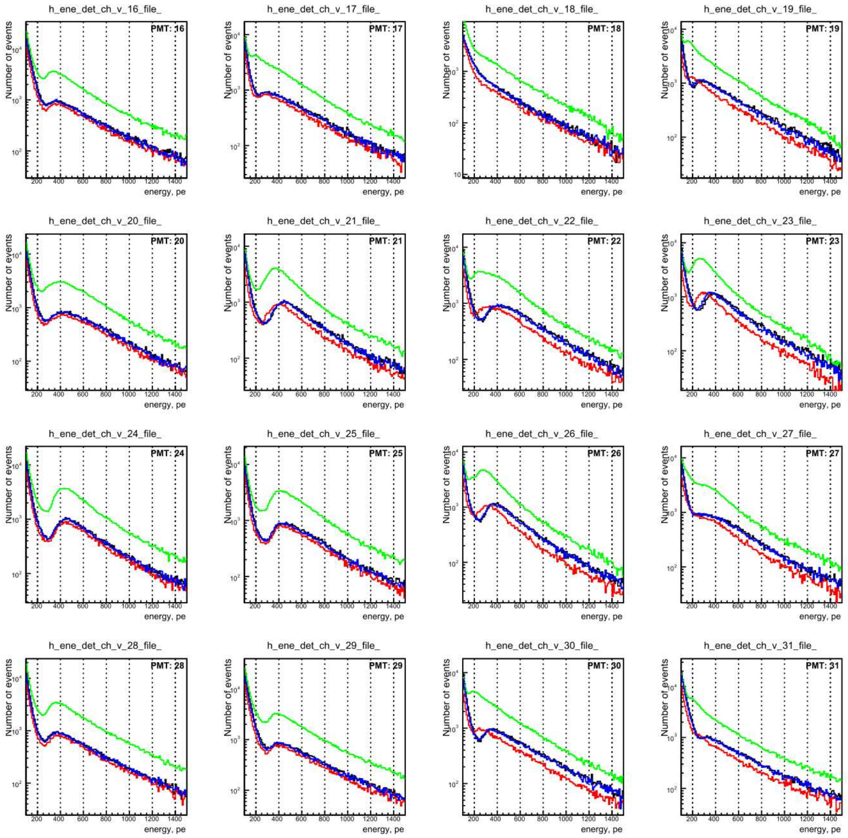

Figure A.2: Energy histograms of muon-tagged events recorded by individual PMT channels for 3 separate weeks: from June 27 to July 3, 2013 on level 6, in black; from September 25 to October 1, 2013 on level 6, in red; from January 24 to January 30, 2014 on level 2, in green. Each of those week data corresponds to what later will be identified in the text as templates T1, T2, and T3 respectively.

is what allows using this template method.

The x-axis of the templates are limited to include only the muon bump, and exclude the gamma exponential at low energies since the position of the gamma-to-muon valley should vary depending on the underground depth and local gamma background. The tail end of the spectra at large energies is also excluded as we are interested in getting accurate values of the gain corrections near the energy threshold at lower energies. In this method we assume that the gain corrections are linear over the full energy range.

A.0.3 Analysis

We analyzed two datasets collected at two different KURF mine levels. The first data set was collected at level 6, at 600 m.w.e., from June 27th , to December 9th, 2013. The second dataset was collected at the shallower level 2, at 380 m.w.e., from December 13th, 2013 to May 2nd, 2014, with a gap of about a month starting on December 19th caused by a failure in the high voltage power supply system

We observed that the gains shifts could be separated in three periods of continuous and slow gain drift separated by two discontinuous changes in the data. The first discontinuity occurred on September 20th, when MARS was still collecting data on level 6. After a four-day gap in data collection, the spectral shape of few PMT channels was altered with respect to the week-one templates, which we will identify from now on as templates T1. We believe this was caused by a partial failure of high voltage power supplies as they became contaminated with diesel soot from the mine. Thus, we created another set of templates for all PMT channels, named templates T2, using the data of the week starting on September 25th, 2013, and fitted those to the remaining of the data collected on level 6. See Fig. A.3 for an example of fitting template T1 to a week of data in the first period (June 27 to September 19, 2013) . Figure A.4 contains an example of a week of data in the second period (September 25 to December 9, 2013) fitted with template T2.

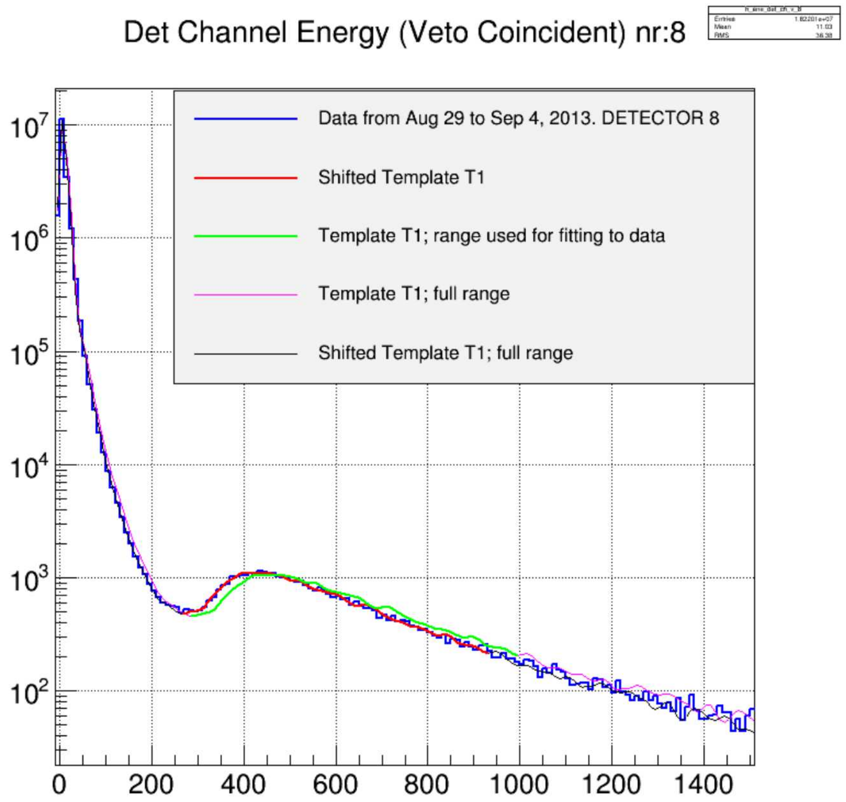

Figure A.3: Detector 8 histogram as an example of a week of data fitted to template T1. In blue is the data of week from August 29 to September 4, 2013. In green is the range of template T1 that was fitted to data, and in pink is the full range of template T1 as reference. In red (and in black for the full energy range) is template T1 shifted by the gain correction, which correctly overlaps with data.

The second data change occurred when the system was moved to level 2. Since level

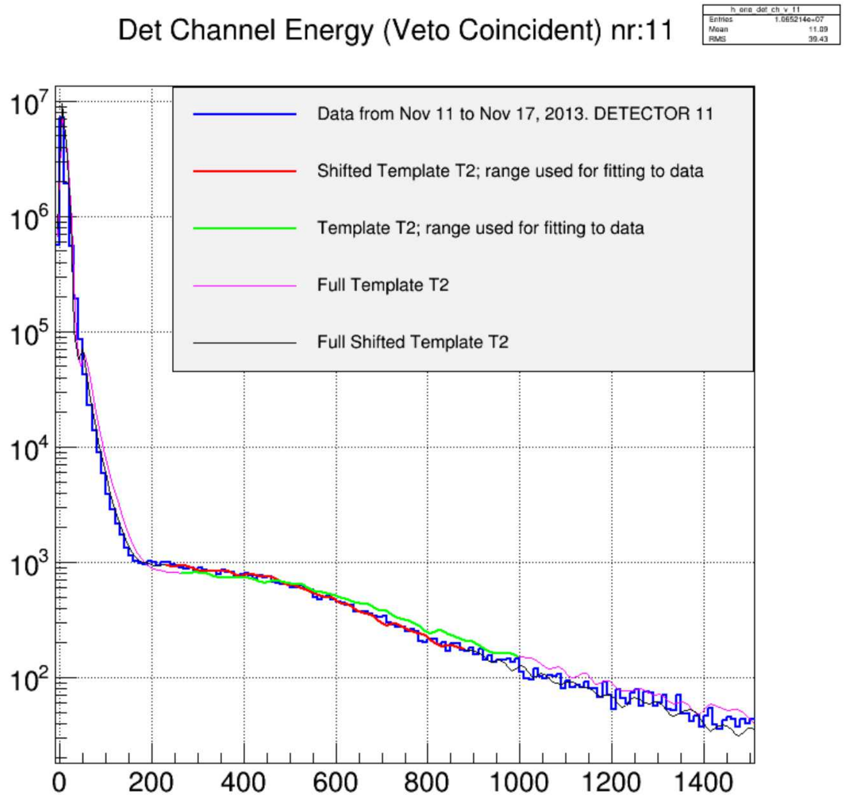

Figure A.4: Detector 11 histogram as an example of a week of data fitted to template T2. In blue is the data of week from November 11 to November 17, 2013. In green is the range of template T2 that was fitted to data, and in pink is the full range of template T2 as reference.

2 is at shallower depth, the muon flux is larger and consequently, the muon feature was larger and with slightly different shape due to a higher muon to gamma ratio. Also, the spectral profile for few PMT channels was again altered, probably due to hardware issues such as partial decoupling of the PMTs from the light guides that occurred as the detector was shaken in the trailer during the move. Therefore, we created a new set of templates T3 using the data of the week starting on January 24, 2014, when data collection at level 2 became stable, and fitted them to all level 2 data. See Fig. A.5 for an example of fitting template T3 to a week of data in the third period (January 17, 2013 to April 28, 2014).

In order to stitch together the results for the three periods described above and provide an overall gain correction with respect to the start date, the best fits of templates T1 to the templates T2 (Figs. A.6 and A.7) and templates T3 (Figs. A.8 and A.9) were computed, despite some variation in PMT shape between the different period templates. These provided gain corrections for the beginning of each period with respect to the initial gain, that were multiplied by the respective gain corrections with respect to T2 and T3 to get the overall gain corrections.

Figure A.10 shows the overall gain corrections of all PMT channels computed at one-

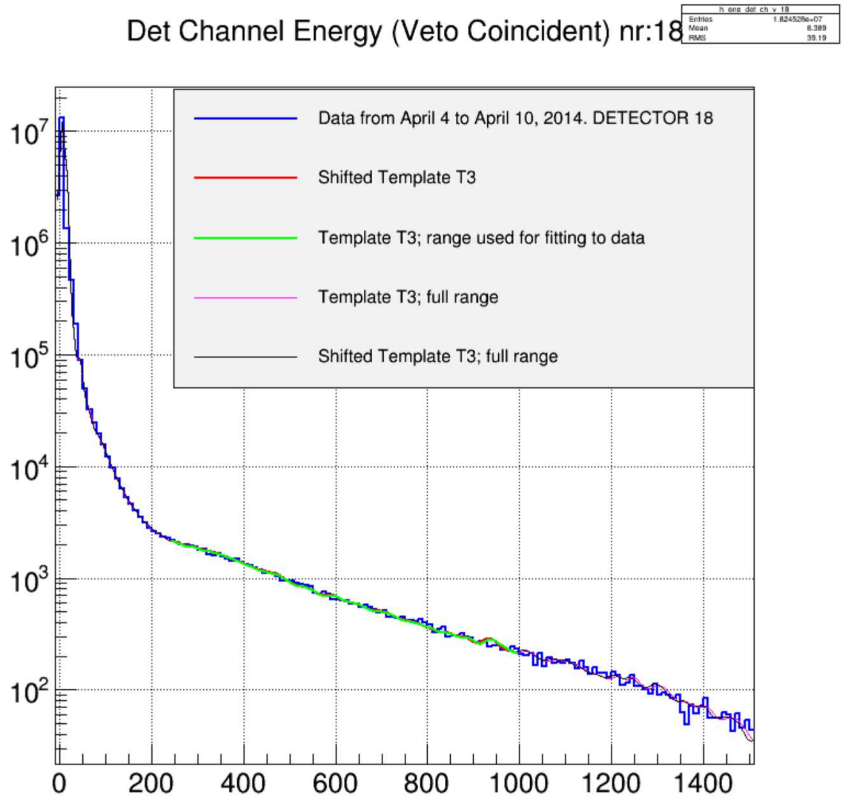

Figure A.5: Detector 18 histogram as an example of a week of data fitted to template T3. In blue is the data of week from April 4 to April 10, 2014. In green is the range of template T3 that was fitted to data, and in pink is the full range of template T3 as reference. In red (and in black for the full energy range) is template T3 shifted by the gain correction, which correctly overlaps with data.

week intervals, where the horizontal axis indicates the number of days since data starts on June 27th. When generating these graphs, we eliminated the cases for which the fits did not succeed, and therefore there can be gaps longer than a week between some x-axis points. On level 2, during period one (from day 0 to day 83), the gain drifts continuously for most PMT channels. Then, there is an abrupt change in several PMT channels from period 1 to period 2, followed by continuous gain drifts during period 2, from day 90 to day 165. The third period on level 2 starts on day 204, after an abrupt change in gain for some PMT channels, but then it becomes relatively stable. These plots demonstrate our initial statement that the gain drifts are small over weekly time scale.

A.0.4 Results

In the post analysis with the corrected gain, we do not smooth the gain correction graphs of Fig. A.10. Instead, we assign a gain correction value to each day obtained by extrapolating

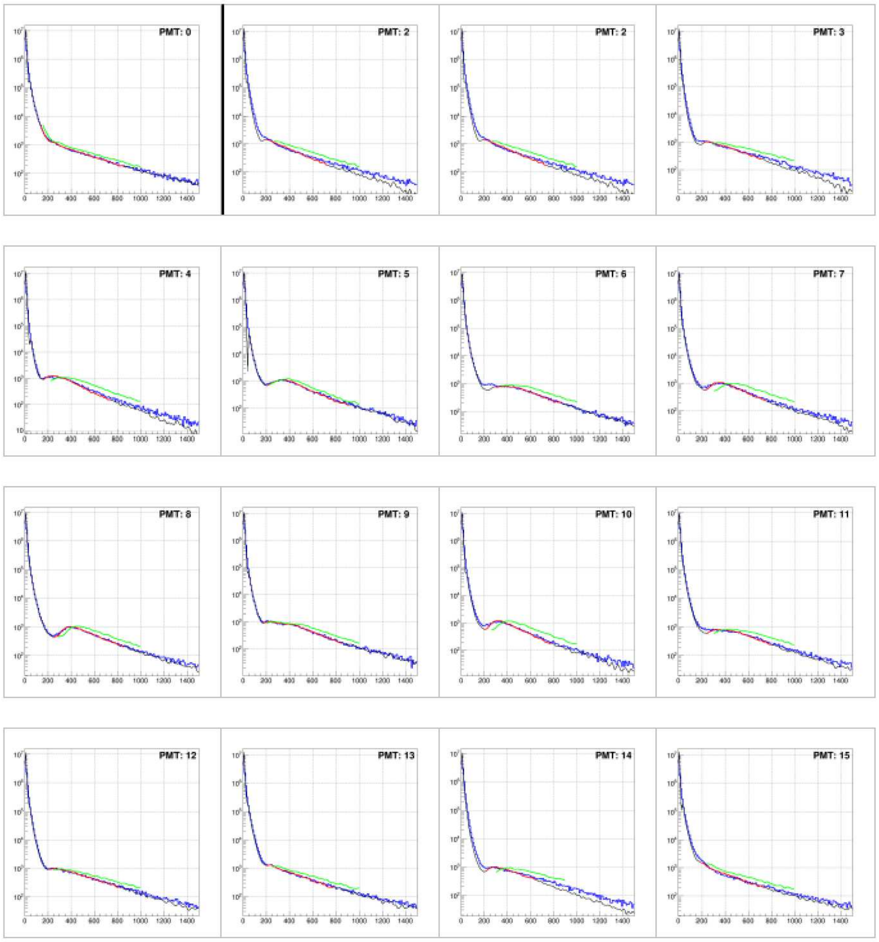

Figure A.6: Computing gains correction of templates T2 with respect to template T1. In blue is the data of the second-period week from September 25 to October 1, 2013, used to create template T2. In green is the range of template T1 that was fitted to data. In red is template T1 shifted by the computed gain correction, in black is the full shifted template T1 as a reference.

between graph points. For comparison, we first show in Figs. A.11 and A.12 the misaligned data, before grain correction, corresponding to 3 separate weeks in the middle of each of the 3 considered periods, plus the data of the start week that we are using as a reference for the gain correction and to set the threshold values. Figure **??**### shows the same weeks after applying the gain corrections calculated above. As desired, the histograms are aligned.

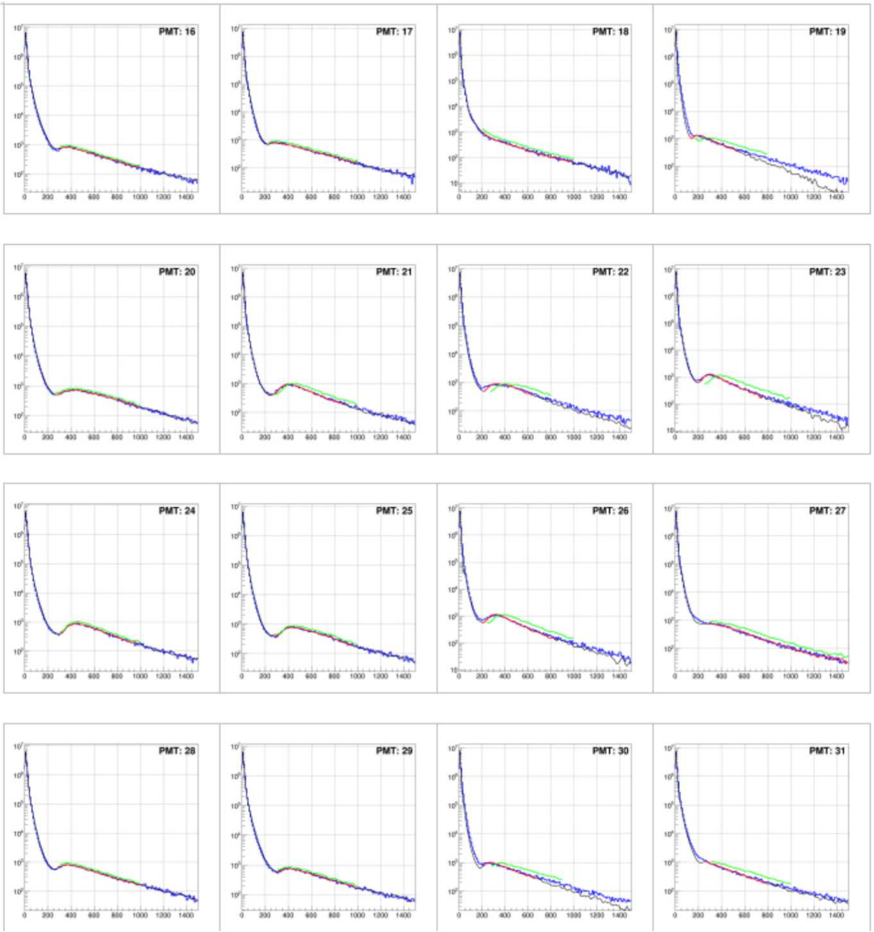

Figure A.7: Computing gains correction of templates T2 with respect to template T1. In blue is the data of the second-period week from September 25 to October 1, 2013, used to create template T2. In green is the range of template T1 that was fitted to data. In red is template T1 shifted by the computed gain correction, in black is the full shifted template T1 as a reference.

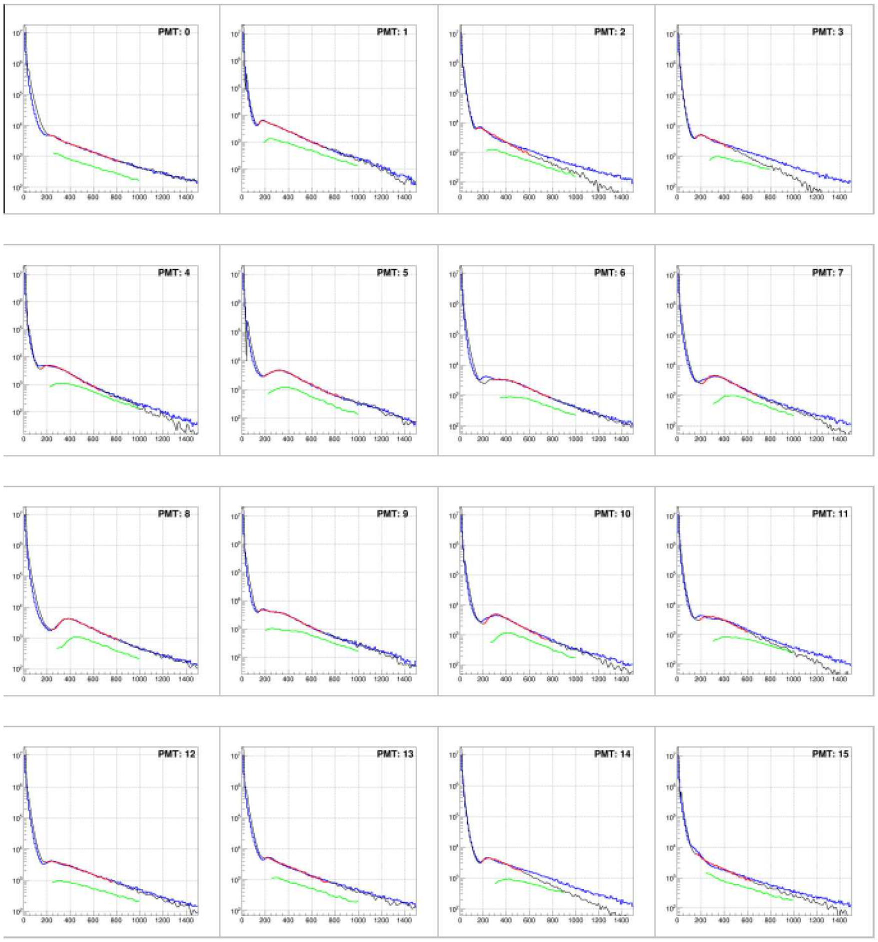

Figure A.8: Computing gains correction of templates T3 with respect to template T1. In blue is the data of the third-period week from January 24 to January 30, 2014, used to create template T3. In green is the range of template T1 that was fitted to data. In red is template T1 shifted by the computed gain correction, in black is the full shifted template T1 as a reference.

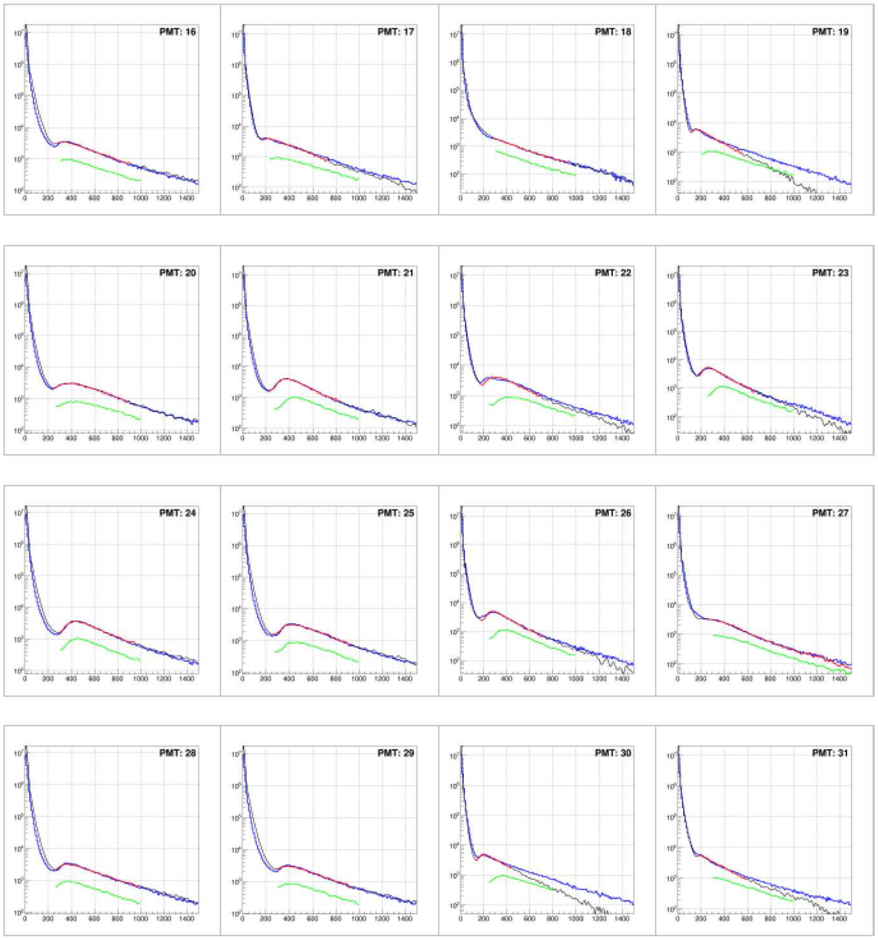

Figure A.9: Computing gains correction of templates T3 with respect to template T1. In blue is the data of the third-period week from January 24 to January 30, 2014, used to create template T3. In green is the range of template T1 that was fitted to data. In red is template T1 shifted by the computed gain correction, in black is the full shifted template T1 as a reference.s

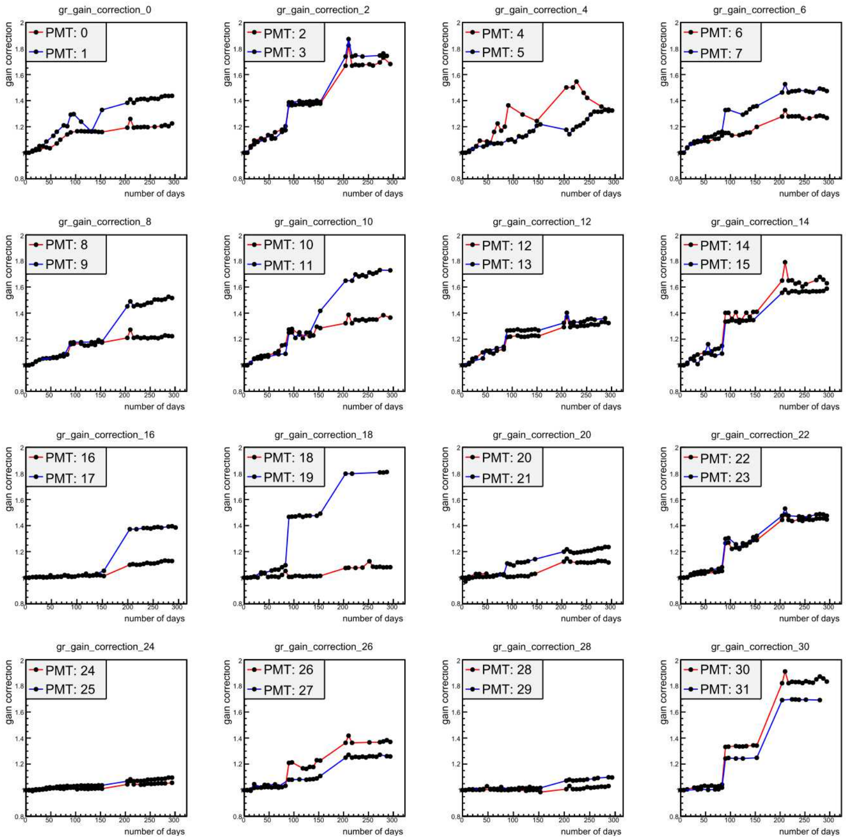

Figure A.10: Gain Correction factor g_c as a function of number of days since the beginning of stable data collection on June 27th, 2013.

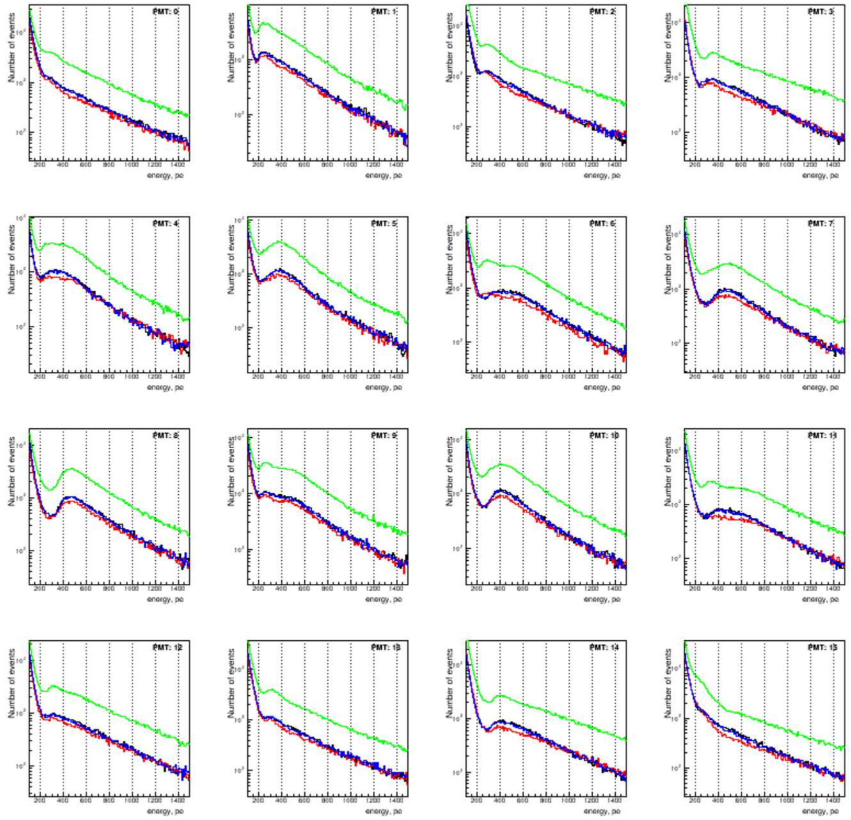

Figure A.11: Pre gain-correction data: start week from June 27 to July 1, 2013 in black, week from August 29 to September 4, 2013 in blue, week from November 11 to November 17, 2013 in red, week from April 4 to April 10, 2014, in green.

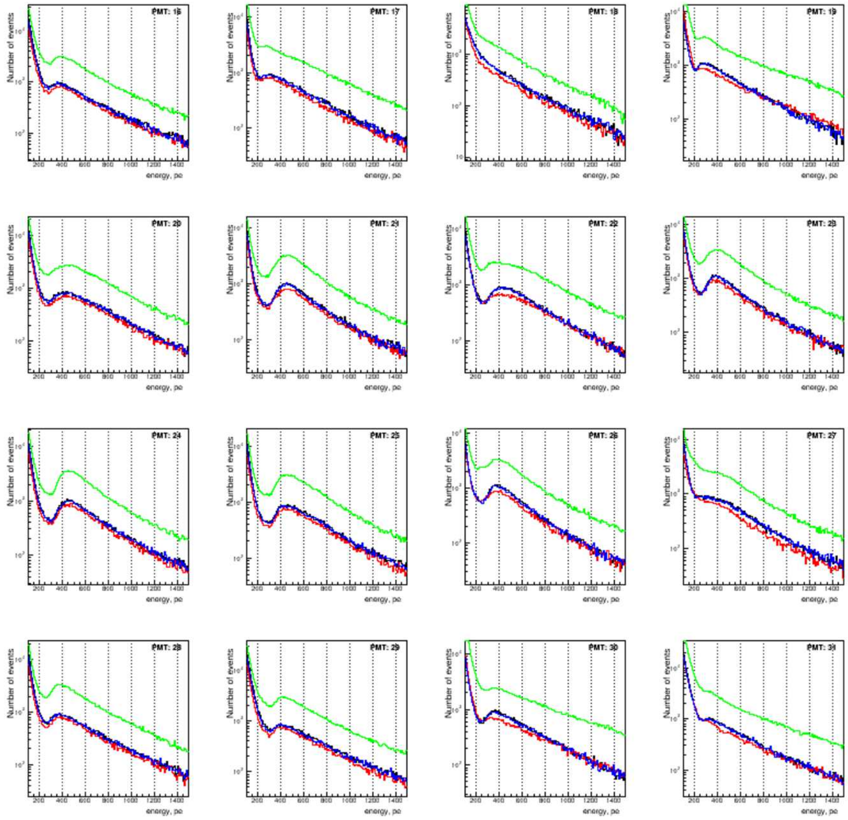

Figure A.12: Pre gain-correction data: start week from June 27 to July 1, 2013 in black, week from August 29 to September 4, 2013 in blue, week from November 11 to November 17, 2013 in red, week from April 4 to April 10, 2014, in green.

Appendix B

Monte Carlo Model and Kernel Creation

The kernel matrix **A** from Eq. 3.1 is created by a Geant4.9.6.p02 Monte Carlo model using the shielding physics list. High energy neutron interactions are carbon are calculated using the MENATE_R package instead of the default Geant4 physics. The model includes the detectors, the lead, the veto system, the trailer with the interior, and a rock volume underneath the trailer (Fig. B.1). Neutrons are thrown from the have sphere above the detector with a cosine distribution. This assumes that the incident neutron spectrum is isotropic; however the detector exhibits a fairly uniform response regardless of the incident neutron direction.

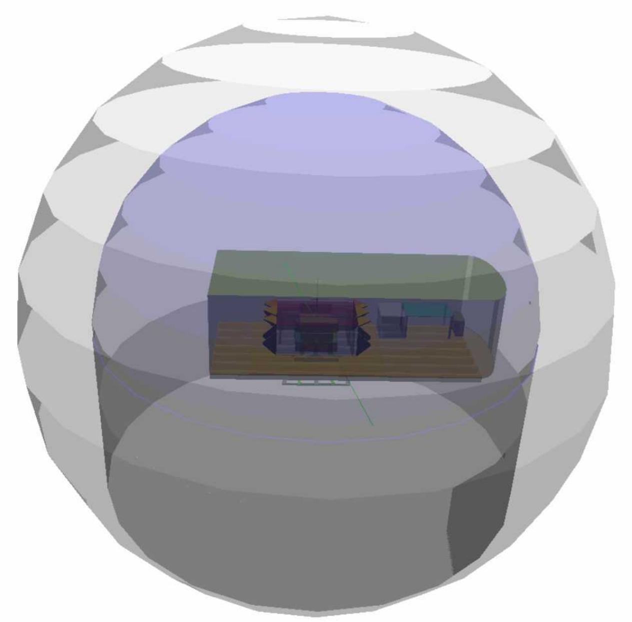

Figure B.1: The Geant4 Monte Carlo model of the MARS detector. The Outer sphere is the simulation volume, the blue half-sphere is the neutron generating surface, the graph cylinder underneath the generating surface is standard rock, and the trailer with all the detector components sits slightly off the rock floor. Neutrons are thrown from the blue generating half-sphere towards the detector in a cosine distribution.

Conceptually the discretization described in Eq. 3.2 is easy to understand if $\vec{y}$ (the measured data space) is a one column vector. However it can be applied to higher dimensions, for example if $\vec{y}$ is a 2 dimensional space (or 3 dimensional as in this experiment):

$$\vec{y} = \begin{bmatrix} a & b \\ c & d \end{bmatrix} \rightarrow \begin{bmatrix} a & c & b & d \end{bmatrix}^T, \tag{B.1}$$

subsequent column vectors can be attached to the end of the preceding column vectors to form a single column vector. Using this discretization the thermalization energy, capture energy, and multiplicity from each incident neutron as well as the initial energy is recorded in kernel matrix where each column corresponds to energy and each row corresponds to some binning of the three parameters,

$$\begin{aligned} \mathbf{A}_{i,j} &= \mathbf{A}_{i,j} + B_j(E) * cos(\theta), && \textbf{iff } \vec{g}_{meas,p} \in \vec{g}_{meas} \\ N_j &= N_j + B_j(E) * cos(\theta), && \textbf{for all } \vec{g}_{meas,p} \end{aligned} \tag{B.2}$$

where the index j corresponds to the basis function number, the index i is fixed by each $\vec{g}_{meas,p}$, θ is the angle from the normal of the generating surface (to produce an isotropic distribution), N is the energy histogram of incident neutrons, and the other quantities have been previously defined. After processing all of the data, each column of $\mathbf{A}$ is divided by the number of incident neutrons with initial energy inside of the energy binning

$$\mathbf{A}_{i,j} = \frac{\mathbf{A}_{i,j}}{N_j}. \tag{B.3}$$

This division of each column incorporates the average intrinsic efficiency of each bin into the kernel matrix. When un-folding with this matrix the result will be counts corrected by intrinsic efficiency.

Appendix C

Regularized MLEM

The Regularization Algorithm

While Eq. 3.6 provides a starting place for solving Eq. 3.2 there exist problems with the solution. Over-convergence is the most serious problem, which results in an oscillatory solution. To alleviate the problem, a regularization can be applied to avoid the non-physical oscillations in the reconstructed spectrum f. Regularization works by applying a penalty (of a-priori knowledge) to Eq. 3.5. The most simple and tried method of regularization is Tikhonov regularization which applies smoothing to the reconstructed spectrum f during the MLEM un-folding[11]. In principle regularized solutions are advantageous if a-priori knowledge of the expected solution exists. A regularized update equation in 1-D can be derived from a paper by De Pierro[12] by defining a new function to minimize

$$\phi(E,\vec{y}) = \Psi(E,\vec{y}) + \beta \sum_{i=0}^{n} R(E), \tag{C.1}$$

where $R(E)$ is a quadratic penalty. In matrix notation:

$$R(E,\vec{y}) = \frac{1}{2}\vec{f}^T \mathbf{C}^T \mathbf{C}\vec{f}, \tag{C.2}$$

where $\mathbf{C}$ is a matrix corresponding to the desired regularization [13]. Two more matrices γ and $\mathbf{K}$, and a vector $\vec{d}$ must be defined:

$$\gamma_{i,j} = \frac{|\mathbf{C}_{i,j}|}{\sum\limits_{k=0}^{k<n} |\mathbf{C}_{i,k}|}, \tag{C.3}$$

$$\mathbf{K}_{i,j} = \frac{\mathbf{C}_{i,j}^2}{\gamma_{i,j}}, \tag{C.4}$$

and

$$d_j^{lk} = \begin{cases} <\mathbf{C}_l, f^k> - \frac{1}{\gamma_{i,j}}\mathbf{C}_{l,j} f_{j,k}, & \gamma_{j,l} \neq 0 \\ <\mathbf{C}_l, f^k>, & \gamma_{j,l} = 0, \end{cases}$$

where $\mathbf{C}$ is the regularization matrix and f^k is the un-folded energy histogram of iteration k. Using the aforementioned matrices and vectors the regularized solution can be found

$$f_j^{k+1} = \frac{(1+\beta\sum_{l=1}^{p}\mathbf{C}_{l,j}d_j^{lk})}{-2\beta\sum_{l=1}^{p}\mathbf{K}_{l,j}} - \frac{\sqrt{(1+\beta\sum_{l=1}^{p}\mathbf{C}_{l,j}d_j^{lk})^2 + 4\beta f_{j,unreg}^{k}\sum_{l=1}^{p}\mathbf{K}_{l,j}}}{-2\beta\sum_{l=1}^{p}\mathbf{K}_{l,j}}, \tag{C.5}$$

where $f_{j,unreg}^{k}$ is the solution of Eq. 3.6, and the other parameters were previously defined.

The Regularization Matrix

Equation C.5 requires the user to choose the regularization matrix $\mathbf{C}$ using a-priori information about the expected solution. This analysis assumes that the final energy spectra will be smooth. In order to produce a smooth solution the difference in the average bin value between two adjacent bins is used to determine all but the first and last rows of $\mathbf{C}$

$$\mathbf{C}_{i+1,j} = \frac{1}{L_{i+1}-L_i}\int_{L_i}^{L_{i+1}} B_j(E)dE - \frac{1}{L_{i+2}-L_{i+1}}\int_{L_{i+1}}^{L_{i+2}} B_j(E)dE, \tag{C.6}$$

where B_j is the basis being used and L_i's are the binned boundaries. The first and last row of the matrix are determined by the difference in the third order derivatives multiplied by the first and last bin width cubed. This is intended to provide a smooth solution near the boundaries.

$$\mathbf{C}_{0,j} = \frac{(L_1-L_0)^3}{L_1-L_0}\int_{L_0}^{L_1} B_j'''(E)dE - \frac{(L_2-L_1)^3}{L_2-L_1}\int_{L_1}^{L_2} B_j'''(E)dE, \tag{C.7}$$

$$\mathbf{C}_{N+2,j} = \frac{(L_{N-3}-L_{N-2})^3}{L_{N-3}-L_{N-2}}\int_{L_{N-2}}^{L_{N-3}} B_j'''(E)dE - \frac{(L_{N-2}-L_{N-1})^3}{L_{N-2}-L_{N-1}}\int_{L_{N-1}}^{L_{N-2}} B_j'''(E)dE, \tag{C.8}$$

where N is the number of basis functions. Once the regularization matrix has been constructed, guessing a β value is still required. To find the optimum regularization value the Euclidean distance between the measured and predicted data space is plotted versus the regularization strength: $||\mathbf{A}\vec{f} - \vec{g}||$ vs. $||\mathbf{C}\vec{f}||$. This plot should in the absence of large background produce a distinctive "L" shape where the corner of the "L" corresponds to the best value. The optimal regularization value produces a predicted data space as close to the measured data space for the smallest regularization strength as possible.

Appendix D

L-Curve Analysis

When MLEM solutions are un-regularized they exhibit over convergence which results in a highly oscillatory solution between adjacent bins. As the regularization parameter β is varied from high to low the solution goes from a flat line, to the optimal solution, to the un-regularized solution. In the flat line case the regularization parameter β is too strong but the value of $||\mathbf{C}\vec{f}||$ is nearly constant. As the solution approaches the optimal β the value of $||\mathbf{C}\vec{f}||$ remains nearly constant but the value of $||\mathbf{A}\vec{f} - \vec{g}_{meas}||$ decreases. Graphically this corresponds to the forward predicted measured data space more closely matching the actual measured data space. As this optimal β is found and continues decreasing the value of $||\mathbf{C}\vec{f}||$ begins to rapidly increase. This happens because the solution begins to oscillate. To find the optimal solution one should look for where $||\mathbf{C}\vec{f}||$ and $||\mathbf{A}\vec{f} - \vec{g}_{meas}||$ are at their corresponding minimum. A more detailed an thorough explanation is given in Hansen [14]. Algorithms designed to find the minimum do exist however only for much simpler inversion algorithms (least squares, SVD, etc.). Here the analysis uses brute force by calculating $||\mathbf{C}\vec{f}||$ and $||\mathbf{A}\vec{f} - \vec{g}_{meas}||$ as a function of β. A user must determine the optimal value from the L-Curve graph.

D.0.5 Simulation

Here the L-Curves for all four simulation cases are presented. The optimal β value is quoted in each figure. When this is used in the analysis the user verified that this is the correct β by running the un-folding algorithm multiple time while Poisson sampling the simulated measured data space. As can be seen the optimal β values are very close for all cases and a very distinctive L shape is observed in the left figure for each of the four simulated cases.

D.0.6 Experiment

Here the L-Curves for level 2 and 6 are presented. The optimal β value is quoted in each figure. When this is used in the analysis the user verified that this is the correct β by running the un-folding algorithm multiple time while Poisson sampling the simulated measured data space. As can be seen the optimal β values vary significantly more than the simulated case.

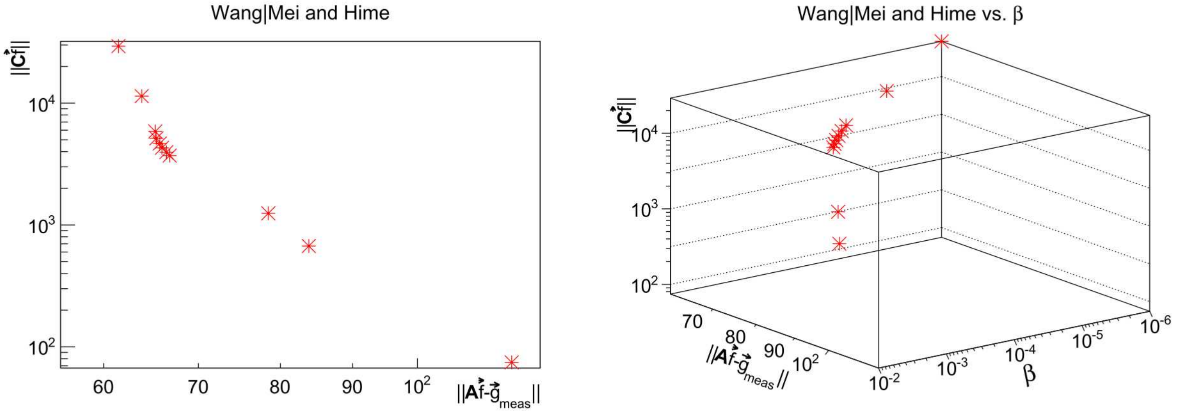

Figure D.1: The parts are labeled A through B from left to right. The figures represent the regularization parameter dependence of the L-curve for the Wang or Mei and Hime simulation. An optimum β value can be observed at the minimum of $6e^{-5}$. Part A is a projection of the β value of Part B onto the L-Curve axis.

Level 2 with superior statistics exhibits a lower optimal β and a more distinctive L shape. Level 6 is quite difficult to discern an L shape. However the optimal β for level 6 of $1e^{-4}$ seems to be correct. While running the un-folding algorithm if the β value was decreased slightly significant oscillations in the solution began to appear.

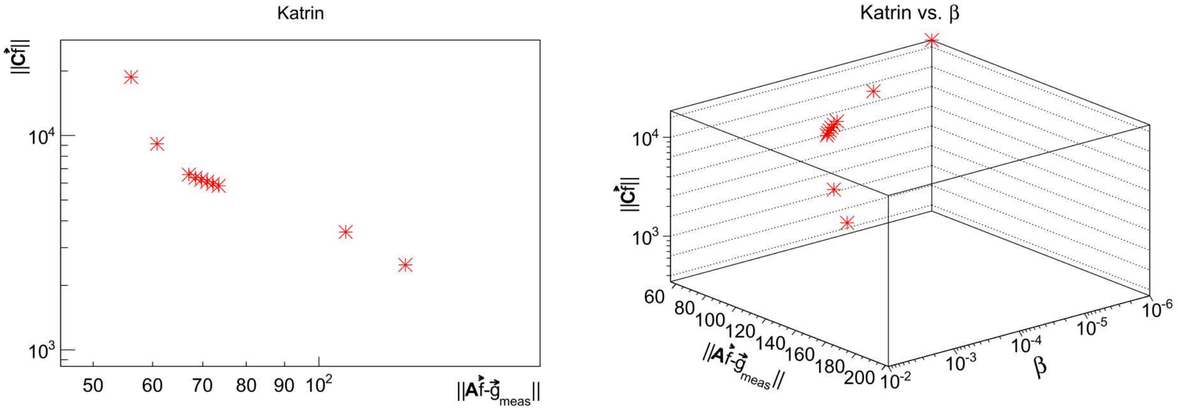

Figure D.2: The parts are labeled A through B from left to right. The figures represent the regularization parameter dependence of the L-curve for the Katrin simulation. An optimum β value can be observed at the minimum of $1e^{-5}$. Part A is a projection of the β value of Part B onto the L-Curve axis.

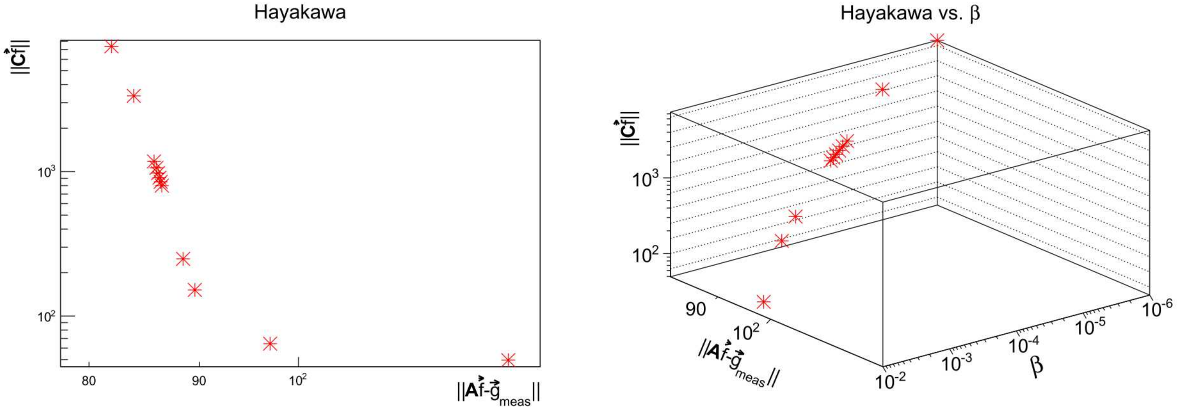

Figure D.3: The parts are labeled A through B from left to right. The figures represent the regularization parameter dependence of the L-curve for the Katrin simulation. An optimum β value can be observed at the minimum of $6e^{-5}$. Part A is a projection of the β value of Part B onto the L-Curve axis.

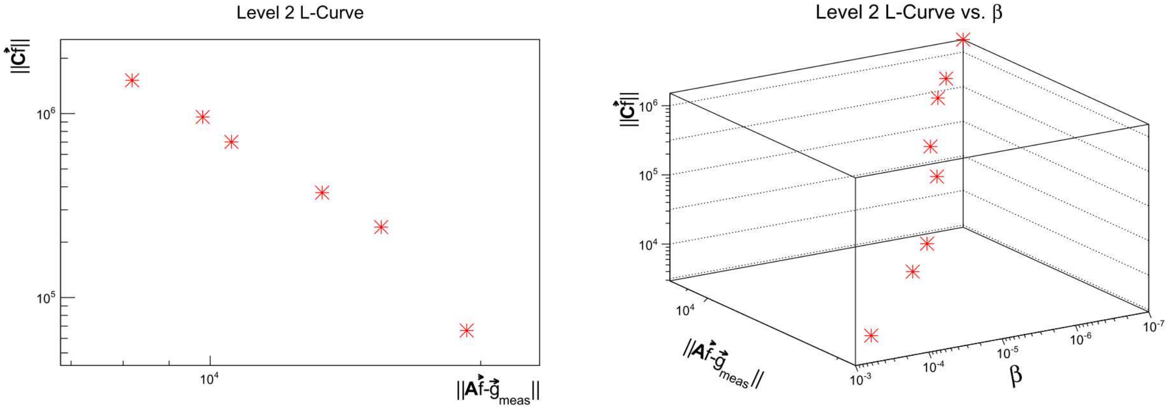

Figure D.4: The parts are labeled A through B from left to right. The figures represent the regularization parameter dependence of the L-curve for the level 2 data. An optimum β value can be observed at the minimum of $5e^{-6}$. Part A is a projection of the β value of Part B onto the L-Curve axis.

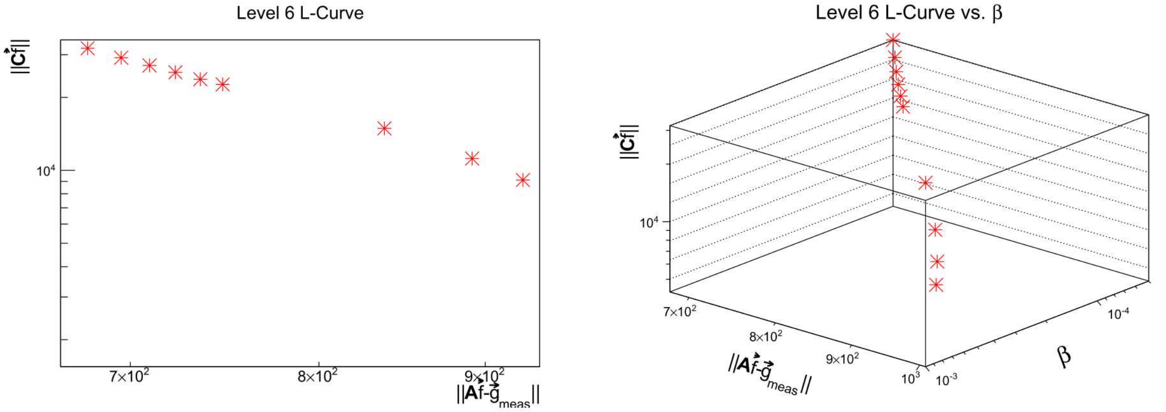

Figure D.5: The parts are labeled A through B from left to right. The figures represent the regularization parameter dependence of the L-curve for the level 6 data. An optimum β value can be observed at the minimum of $1e^{-4}$. Part A is a projection of the β value of Part B onto the L-Curve axis.

Appendix E

Converting MLEM Output to Flux

To produce results comparable to theory the unfolded count value must be converted to intensity or flux. Referring to Eq. B.2 the normalization vector N_j includes particles passing through the detector as well as those interacting. This implies the unfolded count value is the count value corrected for intrinsic efficiency. To convert to intensity the count is divided by the area of the generating surface, the steradian weighting, and the geometric efficiency

$$I_i[n/cm^2/sec/sr] = \frac{f_i}{2\pi R^2 \pi \epsilon_{geo}}, \tag{E.1}$$

where I is the intensity, f_i is the intrinsically corrected counts in a bin divided by the bin width (Eq. 3.2), $2\pi R^2$ is the generating surface area, π is the steradian weighting, and ϵ_{geo} is the geometric efficiency [15]. To convert to flux the intensity is multiplied by the generating surface area weighting by the thrown distribution. Here the distribution is isotropic so the weighting is the surface area which results in a bin dependent flux of

$$F_i[n/cm^2/sec] = 2\pi I_i, \tag{E.2}$$

where F is the flux, and I was defined in Eq. E.1.

DISTRIBUTION:

1	MS 9406	Peter Marleau, 8127
1	MS 9406	Melinda Sweany, 8127
1	MS 9406	Craig Tewell, 8127
1	MS 9292	Ken Patel, 8125
1	MS 9291	Jim Brennan, 8125
1	MS 9291	Dan Throckmorton, 8125
1	MS 9004	Wen Hsu, 8120
1	MS 9004	Jim Lund, 8130
1	MS 0968	Robert Tachau, 5753
1	MS 0899	Technical Library, 9536 (electronic copy)

Sandia National Laboratories